Lithosphere-asthenosphere interaction beneath Ireland from joint inversion of teleseismic P-wave delay times and GRACE gravity

J. P. O'Donnell, E. Daly, Christel Tiberi, I. D. Bastow, B. M. O'Reilly, P. W. Readman, F. Hauser

Geophysical Journal International

Geophys. J. Int. (2011) **184,** 1379–1396 doi: 10.1111/j.1365-246X.2011.04921.x

Lithosphere–asthenosphere interaction beneath Ireland from joint inversion of teleseismic *P*-wave delay times and GRACE gravity

J. P. O'Donnell,[1] E. Daly,[1] C. Tiberi,[2] I. D. Bastow,[3] B. M. O'Reilly,[4] P. W. Readman[4] and F. Hauser[4,5]

[1] *Earth and Ocean Sciences, School of Natural Sciences, National University of Ireland, Galway, Ireland. E-mail: johnpaulodonnell@gmail.com*
[2] *Géosciences Montpellier, UMR* 5243 - CC 60, *Université Montpellier* 2, *Place E. Bataillon,* 34095 *Montpellier cedex* 5, *France*
[3] *Department of Earth Sciences, University of Bristol, Bristol* BS8 1RJ, *UK*
[4] *Dublin Institute for Advanced Studies,* 5 *Merrion Square, Dublin* 2, *Ireland*
[5] *UCD School of Geological Sciences, University College Dublin, Belfield, Dublin* 4, *Ireland*

Accepted 2010 December 10. Received 2010 November 24; in original form 2010 July 21

SUMMARY

The nature and extent of the regional lithosphere–asthenosphere interaction beneath Ireland and Britain remains unclear. Although it has been established that ancient Caledonian signatures pervade the lithosphere, tertiary structure related to the Iceland plume has been inferred to dominate the asthenosphere. To address this apparent contradiction in the literature, we image the 3-D lithospheric and deeper upper-mantle structure beneath Ireland via non-linear, iterative joint teleseismic-gravity inversion using data from the ISLE (Irish Seismic Lithospheric Experiment), ISUME (Irish Seismic Upper Mantle Experiment) and GRACE (Gravity Recovery and Climate Experiment) experiments. The inversion combines teleseismic relative arrival time residuals with the GRACE long wavelength satellite derived gravity anomaly by assuming a depth-dependent quasilinear velocity–density relationship. We argue that anomalies imaged at lithospheric depths probably reflect compositional contrasts, either due to terrane accretion associated with Iapetus Ocean closure, frozen decompressional melt that was generated by plate stretching during the opening of the north Atlantic Ocean, frozen Iceland plume related magmatic intrusions, or a combination thereof. The continuation of the anomalous structure across the lithosphere–asthenosphere boundary is interpreted as possibly reflecting sub-lithospheric small-scale convection initiated by the lithospheric compositional contrasts. Our hypothesis thus reconciles the disparity which exists between lithospheric and asthenospheric structure beneath this region of the north Atlantic rifted margin.

Key words: Gravity anomalies and Earth structure; Body waves; Seismic tomography; Dynamics of lithosphere and mantle; Europe.

1 INTRODUCTION

The tertiary formation of the north Atlantic has regularly been cited as the type example of continental breakup above a mantle thermal anomaly (e.g. White & McKenzie 1989). Wide-angle seismic studies have provided detailed constraints on the regional lithospheric structure (e.g. Barton 1992; O'Reilly *et al.* 1998; Chadwick & Pharaoh 1998; White *et al.* 2008), but constraints on present day lithosphere–asthenosphere interactions are relatively lacking. Situated near the rifted margin, Ireland represents an ideal locale to study such processes because, although tectonically stable today, the geological record there documents a long tectonic history from Precambrian basement formation, through the Caledonian Orogeny, to Paleogene magmatism associated with the breakup of Pangaea.

Studies of lithospheric structure in Ireland and the British Isles using seismic refraction (e.g. Hauser *et al.* 2008; O'Reilly *et al.* 2010), seismic anisotropy (e.g. Helffrich 1995; Do *et al.* 2006; Bastow *et al.* 2007), receiver functions (e.g. Tomlinson *et al.* 2006; Di Leo *et al.* 2009), gravity (e.g. Readman *et al.* 1997) and magnetotellurics (e.g. Rao *et al.* 2007) show that ancient (principally Caledonian) structures still dominate, up to hundreds of millions of years after formation. Studies of the uppermost mantle (∼30–300 km), however, cite low-velocity anomalies imaged using *P*-wave teleseismic tomography (e.g. Arrowsmith *et al.* 2005; Wawerzinek *et al.* 2008) and forward and inverse modelling of gravity and wide-angle seismic data (Al-Kindi *et al.* 2003) as evidence that hot, partially molten plume material from Iceland presently resides beneath lithospheric thin-spots in this region of the north Atlantic rifted margin. However, absolute traveltimes of teleseismic phases in Ireland and Britain are notably fast compared to the global average (e.g. Poupinet 1979; Poupinet *et al.* 2003; Amaru *et al.* 2008), with the implication that low velocities imaged using relative arrival time methods (e.g. Arrowsmith *et al.* 2005; Wawerzinek *et al.* 2008) may not be, as has previously been assumed, genuinely 'slow'. The present day

plume hypothesis may then be inappropriate for the mantle in this region, in which case we must look beyond the 'red=hot mantle, blue=cold mantle' first-order explanation. Ireland is tectonically quiescent, has a largely flat Moho (e.g. Landes *et al.* 2005), a relatively low lithospheric elastic thickness (e.g. Armstrong 1997; Daly *et al.* 2004), little topography and yet the lithosphere and uppermost mantle are evidently heterogeneous. Second-order anomaly sources which cannot so readily be explained may have to be considered.

We address these issues by using data from the ISLE (Irish Seismic Lithospheric Experiment), ISUME (Irish Seismic Upper Mantle Experiment) and GRACE (Gravity Recovery and Climate Experiment) experiments to perform a joint teleseismic-gravity inversion for Ireland's lithospheric and uppermost mantle structure. Compared to traditional terrestrial gravity surveys, the long wavelength GRACE data can probe lithospheric mantle structure, and has been used, for example, to infer the topography of the very deep Moho (extending to ∼80 km) beneath the Tibetan plateau (Shin *et al.* 2007, 2009), the structure of the European mantle lithosphere (Tesauro *et al.* 2007) and the lithosphere-asthenosphere boundary (LAB) beneath the Red Sea and Arabian Peninsula (Hansen *et al.* 2007). By incorporating GRACE gravity data within a joint inversion scheme and drawing on increased seismic resolution relative to the previous tomographic study of Ireland's uppermost mantle (Wawerzinek *et al.* 2008), we seek to resolve the disparity that exists in the literature regarding a lithosphere pervaded by Paleozoic signatures overlying an asthenosphere purportedly dominated by tertiary structure.

2 TECTONIC SETTING

Ireland's present day geological structure is considered to reflect four principal tectonic events: the Caledonian Orogeny, the Variscan Orogeny, the opening of the North Atlantic Ocean and the initiation of the proto-Iceland plume. The crustal fabric is dominated by Caledonian and Variscan trends (e.g. Readman *et al.* 1997; Restivo & Helffrich 1999). The pervasive NE–SW Caledonian trend is the result of a major tectonic event that culminated in late Ordovician and Silurian times with the closure of the Iapetus Ocean (e.g. Woodcock & Strachan 2000). The Iapetus suture marks the continent–continent collision, and purportedly runs in an approximately northeastward direction from the present day Shannon estuary in the west of Ireland, across the Irish Midlands, and into the Scottish Highlands (e.g. Phillips *et al.* 1976; Woodcock & Strachan 2000) (ISZ; Fig. 1). Variscan deformation in Ireland is characterized by east–west oriented thrusts, a result of the dominant northward directed compression of the latter phases of the orogeny (e.g. Cooper *et al.* 1986). The Variscan trend is most evident in the south of the country, becoming less apparent in central and northern regions (e.g. Gill 1962; Masson *et al.* 1999). Post-Variscan tectonic activity was dominated by the protracted opening of the Atlantic Ocean, believed to be related to the formation of the series of Mesozoic basins and fault-bounded troughs offshore western Ireland (e.g. Naylor & Shannon 2009). Paleogene magmatism associated with the British Tertiary Volcanic Province (BTVP) produced the volcanic features across northern Ireland, including the Mourne, Carlingford and southern Slieve Gullion granitic intrusions (M, C, SG; Fig. 1). White & McKenzie (1989) suggested that the volcanism resulted from localized rifting above the 1000 km radius mushroom head of anomalously hot mantle carried up by the proto-Iceland plume, a hypothesis supported by geochemical and geochronological evidence (e.g. Mussett *et al.* 1988; Barrat & Nesbitt 1996; Gamble *et al.* 1999; Kirstein & Timmerman 2000).

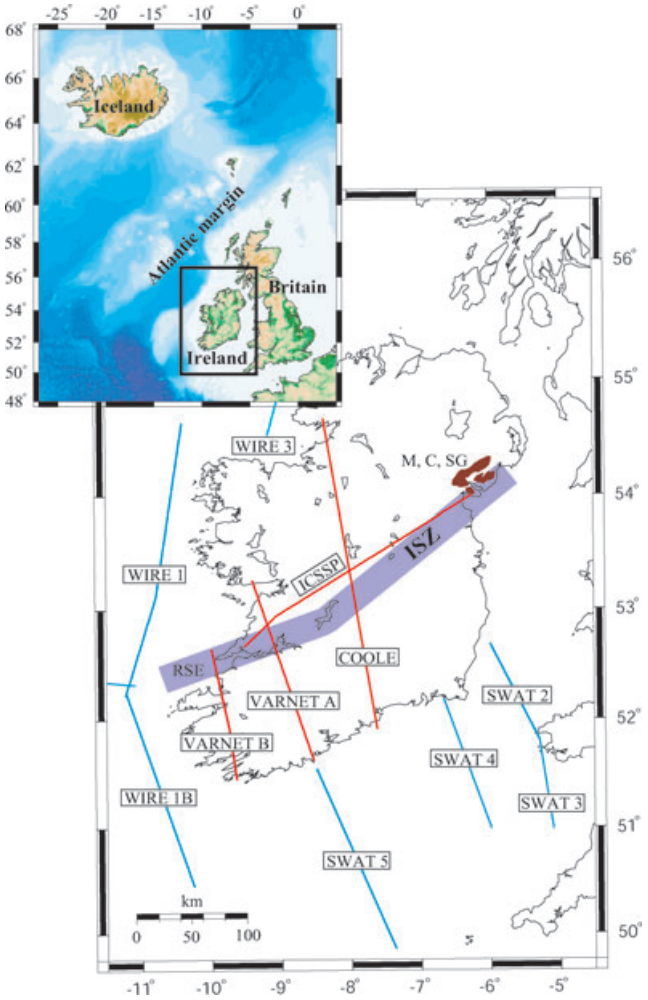

Figure 1. The study area with locations of previous seismic experiments. Onshore wide-angle seismic reflection profiles VARNET A and B (e.g. Masson *et al.* 1999), ICSSP (Jacob *et al.* 1985) and COOLE (Lowe & Jacob 1989) are indicated as red lines. Blue lines are BIRPS offshore marine reflection profiles (SWAT 2–5 and WIRE 1, 1B and 3) from Klemperer & Hobbs (1991). ISZ, Iapetus Suture Zone; RSE, River Shannon Estuary; M, C, SG, Mourne, Carlingford and Slieve Gullion Tertiary central complexes. The inset shows the regional tectonic setting on a topographic map (modified from O'Reilly *et al.* 2010).

3 DATA

3.1 ISLE and ISUME data

Our seismic data came from 18 temporary broadband Güralp CMG-40T seismometers deployed as part of the ISLE/ISUME network (Fig. 2), 15 of which recorded at a sample rate of 75 samples per second (s.p.s.) and three at 25 s.p.s. Additional data were sourced from permanent broadband stations DSB (part of the GEOFON network) and VAL (operated by the Irish Meteorological Office). The instrument at station DSB is a Streckeisen STS-2 and that at station VAL a Güralp CMG-40T, both recording at 75 s.p.s.

For the period 2003 September to 2006 November, a list of 1229 candidate earthquakes with magnitudes mb $\geq$ 5.4 was obtained from the Advanced National Seismic System (ANSS) online catalogue (http://www.ncdec.org/anss/). Of these, 263 earthquakes in the epicentral distance (Δ) range $30^\circ < \Delta < 100^\circ$ (including one originating between $25^\circ < \Delta < 30^\circ$ admitted to fill a backazimuthal gap)

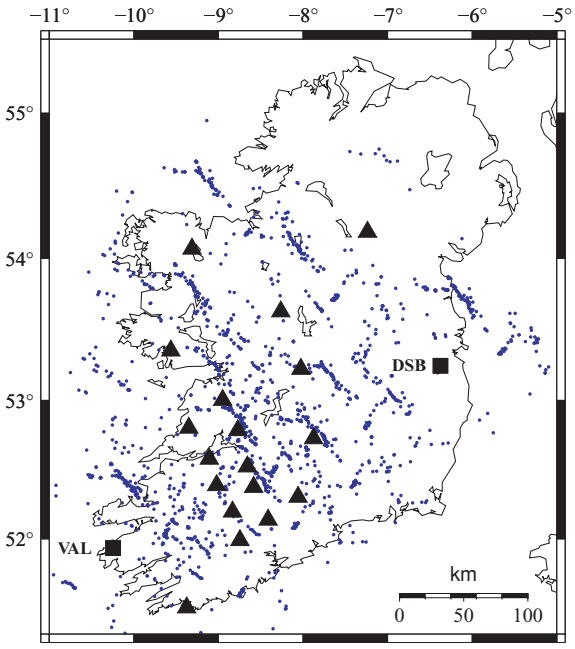

Figure 2. The subset of the ISLE/ISUME network used in this study. Stations VAL and DSB are permanent broad-band stations of the Irish seismic network. The triangles represent DIAS temporary broad-band stations. The blue dots show the piercing points of teleseismic ray paths at a depth of 120 km.

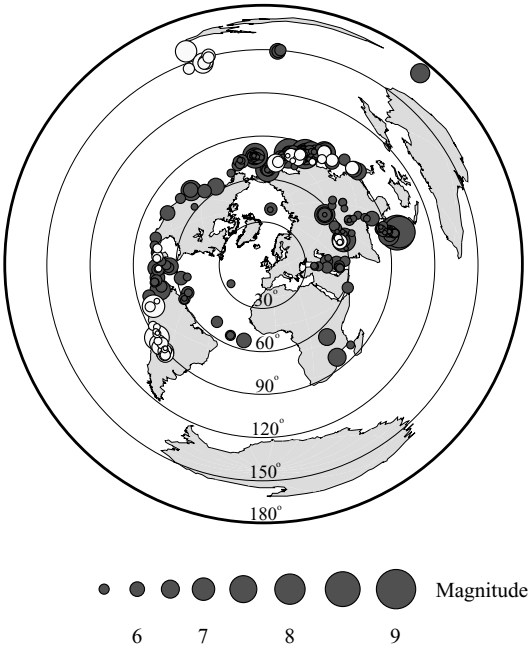

Figure 3. Backazimuthal and epicentral distance distribution of the 276 events used in this study which were recorded over 3 years of the ISLE/ISUME experiment. Forty-eight events have hypocentral depths exceeding 100 km (white discs). The magnitude range is mb 5.4–9.0. Concentric circles are at 30° intervals from the centre of the projection at 8°W, 53°N.

and a further 13 in the epicentral distance range $145^\circ < \Delta < 180^\circ$ yielded high signal-to-noise ratio waveforms at five or more stations for *P* waves and *PKP* core phases, respectively. Fig. 3 shows the distribution of these earthquakes. Backazimuthal coverage is relatively uniform apart from between 90° and 180°. This region (e.g. the Indian Ocean and the South Atlantic) produces only small numbers of low-magnitude poor-quality earthquakes, generally unsuitable for analysis.

3.2 Relative arrival time residuals

Prior to phase picking, each seismogram was passed through a butterworth bandpass filter of order 1, with corner frequencies 0.7 and 2.2 Hz, for visual inspection. Preliminary arrival times were then picked on a peak or trough within the first cycle of coherent energy of the desired phase. This pick was used to define a correlation window (3 s) around the phase arrival, from which accurate relative arrival times with quantitative uncertainty estimates were determined using the multichannel cross-correlation (MCCC) method of VanDecar & Crosson (1990). Relative arrival time residuals were subsequently determined by subtracting similarly normalized theoretical relative arrival times, based on the IASP91 traveltime tables (Kennett & Engdahl 1991), from the MCCC-derived relative arrival times. These residuals are considered to comprise the effects of velocity anomalies residing within the target volume beneath the seismic network only (e.g. Evans & Achauer 1993).

The 276 earthquakes used in this study yielded 1934 relative arrival time residuals. These lie approximately in the range ±0.7 s and have a standard deviation of ∼0.2 s. This compares with an average MCCC estimated picking error of ∼0.05 s. In line with the studies of Tilmann *et al.* (2001) and Bastow *et al.* (2005, 2008), we regard the MCCC derived estimates of picking uncertainty as optimistic. Analysis of the residuals indicates a consistent change from early to late residuals (∼ −0.5 s → 0. 5 s) in moving from north to south across the proposed Iapetus suture zone in southwest Ireland, a finding in agreement with the residual traveltime analysis carried out by Masson *et al.* (1999) based on an earthquake in the Aleutians and a Chinese nuclear test.

3.3 GRACE gravity

The second data set we used was the gravity anomaly derived from the GRACE geopotential model GGM02C (Tapley *et al.* 2005). The GGM02C model consists of a weighted combination of GGM02S and EGM96 spherical harmonic coefficients (Lemoine *et al.* 1998; Tapley *et al.* 2005) and retains correct spectral power at all estimated degrees up to the 200 limit.

The gravity anomaly derived from the GGM02C geopotential model treats all mass as if internal to a regularized geoid, and can therefore be regarded as a Helmert condensation anomaly, of which the free air anomaly is an approximation (e.g. Heiskanen & Moritz 1967). It is distributed as a 30 min grid by the University of Texas at Austin, Center for Space Research (http://www.csr.utexas.edu/grace/). The estimated accumulated error in the GGM02C gravity model increases from about 1.5 mGal at degree 120 (wavelength ∼330 km) to about 5 mGal at degree 200 (wavelength ∼200 km). We calculated a Bouguer slab correction with standard densities (2670 kg m^{-3} for land areas, 1643 kg m^{-3} for oceanic areas) using the merged GLOBE (onshore) and ETOP02v2 (offshore) digital elevation models (DEMs) smoothed to remove wavelengths below that of the order of the GGM02C grid spacing. Both DEMs are distributed by the NOAA's National Geophysical Data Center (NGDC). Fig. 4 shows the resulting Bouguer anomaly over Ireland. Anomaly values range from just below zero to about 30 mGal onshore Ireland, increasing offshore to a maximum of

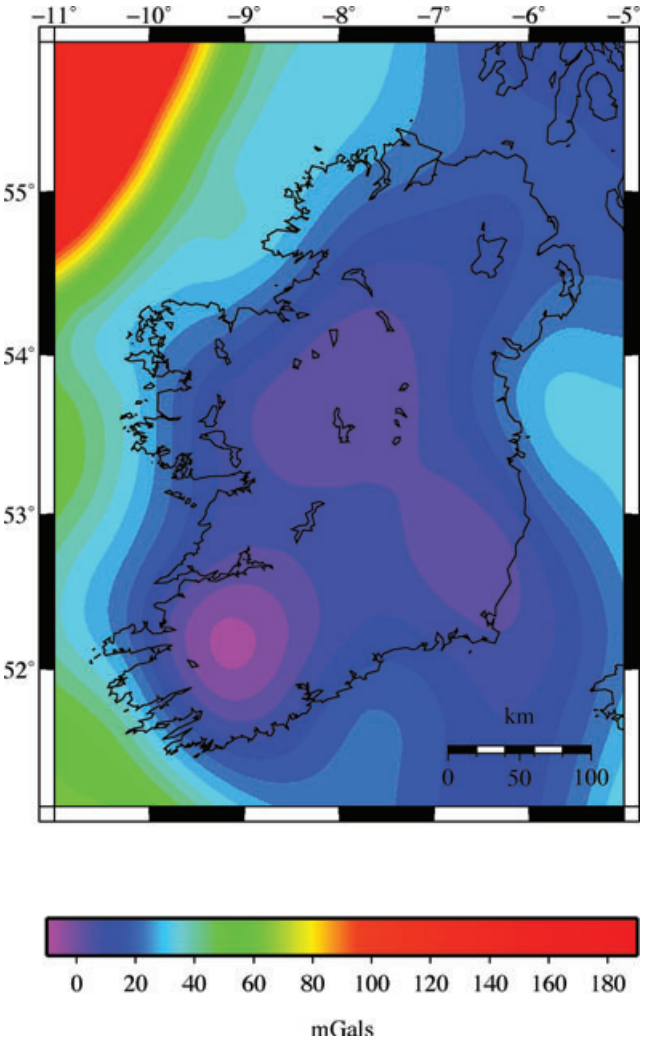

Figure 4. The long wavelength GRACE GGMO2C Bouguer anomaly calculated for Ireland. Anomaly values range from just below zero to about 30 mGal onshore Ireland, which is characterized by three long wavelength Bouguer lows. See text for details.

approximately 180 mGal towards the Atlantic margin. The anomaly onshore Ireland is characterized by three long wavelength Bouguer lows, which broadly correlate with low-velocity anomalies imaged by Wawerzinek *et al.* (2008) in their *P*-wave teleseismic tomographic study of Ireland's uppermost mantle.

The common assumption of isostatic equilibrium at passive margins has been questioned recently (e.g. Moucha *et al.* 2008). However, the relatively low lithospheric elastic thickness determined in the vicinity of the Irish Atlantic margin (e.g. Armstrong 1997; Daly *et al.* 2004) supports the isostatic hypothesis. Consequently, we expect any dynamic contribution to the gravity signal due to mantle flow to be negligible. Following Spector & Grant (1970) and Pawlowski (1995), we used the radially averaged power spectrum of the GRACE Bouguer anomaly to estimate depths of between about 20 and 70 km for the causative sources (Fig. 5). The crustal thickness beneath Ireland is relatively uniform at about 30 km, apart from a slight undulation of the Moho coinciding with the location of, and thought to reflect, the fossilized Iapetus suture zone (e.g. Ford *et al.* 1991; Landes *et al.* 2005; Grad *et al.* 2009). However, unlike Ireland's terrestrial gravity data that are pervaded by short wavelength Caledonian and Variscan crustal signatures (e.g. Readman *et al.*

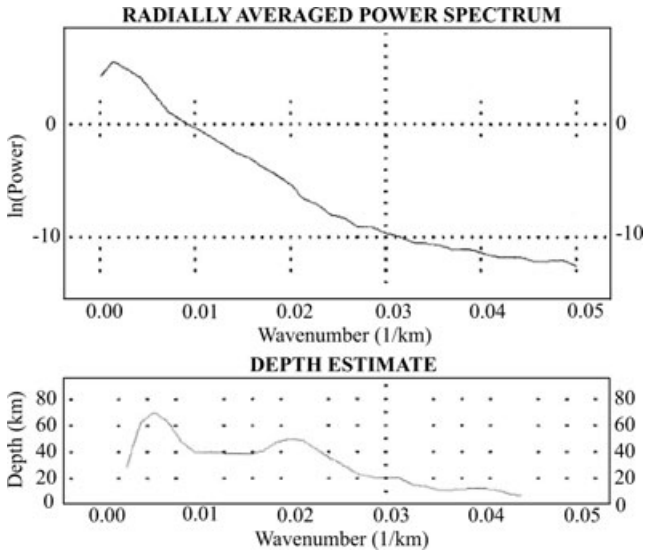

Figure 5. The radially averaged power spectrum of the GRACE GGMO2C Bouguer anomaly with source depth estimates computed using Oasis Montaj^{TM}. Long wavelength sources are estimated to be predominantly located between about 20 and 70 km depth.

1997), the longer wavelength GRACE gravity anomalies exhibit no discernible correlation with Caledonian or Variscan trends, and in particular, the Iapetus suture. The GRACE gravity data thus reflect causative source depths and wavelengths that are expected to be commensurate and coherent with upper-mantle seismic anomalies.

4 METHOD

4.1 Joint inversion

As a function of ray crossing, teleseismic tomographic resolution increases with depth, with shallow (typically crustal) regions suffering from a lack of resolution due to the dearth of ray crossing there. In comparison, the terrestrial gravity survey has traditionally offered optimal resolution at crustal depths (e.g. less than 30 km). The advent of satellite gravimetry has, however, produced gravitational geopotential models that, for certain spherical harmonic degrees (e.g. ∼degree 200 in this study), can both compensate for and overlap with the resolution domain of teleseismic tomography. Such data sets are ideally suited to a cooperative inversion scheme because the complementary information reduces inherent ambiguity or non-uniqueness (e.g. Haber & Oldenburg 1997). Joint inversion treats the data sets simultaneously by placing them into a single data vector to produce model parameter estimates consistent with all data. The principal difficulty with this approach lies in determining a prescription for relating the independent data sets (Lees & VanDecar 1991).

The algorithm used here, developed by Tiberi *et al.* (2003) and Jordan (2003), is based on an algorithm proposed by Zeyen & Achauer (1997) for the joint inversion of teleseismic relative arrival time residuals and Bouguer gravity anomalies. Zeyen & Achauer (1997) invoke the empirical Birch's law (Birch 1961) in prescribing a linear relationship between density and velocity anomalies. The widespread success of Birch's law can be ascribed to its virtual coincidence with, and hence linearization of, a power law derived from lattice dynamics over the density range ∼2.5–4.0 g cm^{-3}, which encompasses most lithospheric rocks and minerals (e.g. Chung 1972). Zeyen & Achauer (1997) consider the velocity–density

relationship depth dependent and allow local deviations from it within individual model layers. The depth dependence of the correlation coefficient (B-coefficient) seeks to account for its temperature dependence, whereas the permitted local deviations seek to account for additional dependencies on a wide range of factors, such as the presence of fluids or rock type (e.g. Christensen & Mooney 1995).

4.2 Joint parametrization scheme

The model space is parametrized in terms of density blocks, velocity nodes and a B-coefficient linking density and velocity for each horizontal layer (Fig. 6). The single B-coefficient per layer represents a mean value, reflecting the fact that B-coefficients are only approximately known. Although the vertical density and velocity layer boundaries are required to be common in order to be able to define B-coefficients, the horizontal parametrization of the density and velocity models is independent, allowing the models to be tailored to their respective information densities (e.g. Jordan 2003). Thus, the velocity grid spacing is smallest in the immediate vicinity of the seismic network where ray crossing is maximal, whereas the density block sizes reflect the data coverage for particular regions. The forward calculation of the gravity anomaly corresponding to the density model is performed by summing the vertical attraction due to the collection of density blocks within the model (e.g. Li & Oldenburg 1998). For the calculation of traveltimes, the array of velocity nodes is interpolated with a pseudo-linear gradient (Thurber 1983) and 3-D ray tracing applied using the minimum time path algorithm developed by Steck & Prothero (1991).

4.3 The inversion algorithm

The inversion seeks to determine the set of density ($\Delta\boldsymbol{\rho}$) and velocity ($\Delta\mathbf{v}$) perturbations and B-coefficients ($\mathbf{B}$) which simultaneously minimize the difference, in a least squares sense, between the observed ($\mathbf{d}_{\rm obs}$) and calculated ($\mathbf{d}_{\rm cal}$) data. Variations in data accuracy between the data sets are accounted for by incorporating a data weighting matrix, $\mathbf{C}_{\rm d}$, in the inversion scheme. This matrix weights the data by the reciprocal of their variances, such that the most uncertain have the least effect in determining an optimum model. The expression to be minimized is

$$(\mathbf{d}_{\rm obs} - \mathbf{d}_{\rm cal})^{\rm T}\mathbf{C}_{\rm d}^{-1}(\mathbf{d}_{\rm obs} - \mathbf{d}_{\rm cal}), \quad (1)$$

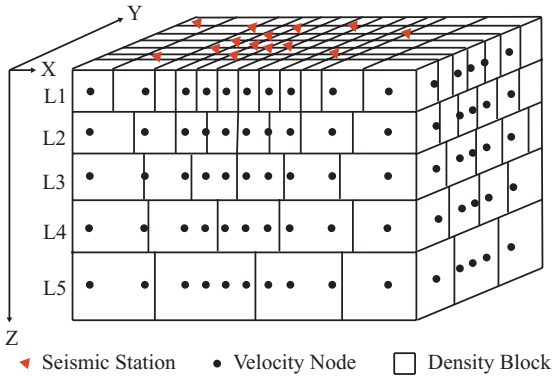

Figure 6. Schematic illustration of the joint inversion parametrization. Each layer L_n is subdivided into density blocks and velocity nodes, and to each layer there corresponds a B-coefficient linking density and velocity. The concentration of blocks and nodes can vary to reflect the respective information densities within the model space (modified from Tiberi *et al.* 2003).

where T denotes the matrix transpose. The inversion will, however, typically be ill-posed, and as such will require regularization. By adopting a Bayesian approach (Jackson & Matsu'ura 1985), *a priori* model parameter estimates, $\mathbf{p}_0$, are directly incorporated in the inversion scheme. Varying degrees of confidence in the *a priori* model parameter estimates are accounted for by incorporating a parameter weighting matrix, $\mathbf{C}_{\rm p}$, in the expression to be minimized. This matrix contains *a priori* model parameter variances which determine how far corresponding model parameters may deviate from initial *a priori* estimates. This damping constraint is imposed by the minimization of the term

$$(\mathbf{p} - \mathbf{p}_0)^{\rm T}\mathbf{C}_{\rm p}^{-1}(\mathbf{p} - \mathbf{p}_0), \quad (2)$$

where $\mathbf{p}^{\rm T} = (\Delta\boldsymbol{\rho}, \Delta\mathbf{v}, \mathbf{B})$ is the sought vector of optimal model parameters.

Zeyen & Achauer (1997) impose two further regularization constraints on the inversion. The first of these is provided by the relationship which defines the joint inversion, Birch's law. A variance matrix, $\mathbf{C}_{\rm b}$, constrains possible deviations of the density–velocity relation from assumed linearity. The smaller a diagonal term variance, the stricter the adherence to the linear density–velocity relation. This density–velocity relation regularization is imposed by minimizing the expression

$$(\Delta\mathbf{v} - \mathbf{B}\Delta\boldsymbol{\rho})^{\rm T}\mathbf{C}_{\rm b}^{-1}(\Delta\mathbf{v} - \mathbf{B}\Delta\boldsymbol{\rho}), \quad (3)$$

which can of course only be applied to those density blocks which are constrained by velocity information.

A final form of regularization is imposed by demanding that the final models exhibit sufficient smoothness so as to be physically plausible. The smoothness constraint is enforced by minimizing the root mean square of the first derivatives of the parameters in each layer

$$\left(\frac{\Delta\mathbf{p}}{\Delta\mathbf{R}}\right)^{\rm T}\mathbf{C}_{\rm s}^{-1}\left(\frac{\Delta\mathbf{p}}{\Delta\mathbf{R}}\right), \quad (4)$$

where $\Delta\mathbf{p}$ is the difference between adjacent parameters separated by a distance $\Delta\mathbf{R}$. The variance matrix $\mathbf{C}_{\rm s}$ controls the importance of this constraint relative to the others.

The total expression to be minimized is therefore the sum of the terms (1)–(4). After linearization, an iterative procedure for estimating optimum model parameters is obtained. A detailed exposition of the linearized equation is given in Zeyen & Achauer (1997).

4.4 Parametrization

Resolution of structure in traveltime tomography improves with depth before degrading beyond a depth commonly quoted as being between two-thirds and one times the length of the seismic network (e.g. Evans & Achauer 1993). As the seismic network in this study extends over an area of approximately 250 km × 320 km, resolution is expected to degrade to an unacceptably poor level somewhere in the depth range ∼250–320 km. The depth extent of the velocity model was thus set at 285 km. The lateral extent of the velocity model was chosen to encompass the area of ray coverage as determined by ray piercing points at various depth slices within the model volume. This was subsequently extended approximately 300 km beyond the data coverage limits in all directions to avoid possible contamination by spurious boundary effects (e.g. Tiberi *et al.* 2003; Allen *et al.* 2002). A possible drawback of this approach is the removal of legitimate structure from the interior region of the model. However, the philosophy is to invert for the minimum structure required to explain the data (e.g. VanDecar *et al.* 1995). The

poorly constrained outer nodes, whose purpose it is to absorb edge effects, are not represented in the final velocity model.

A minimum lateral node spacing of 25 km in the model interior was chosen to reflect the average station spacing in the centre of the seismic array, which is conventional practice in seismic tomography (e.g. Tiberi *et al.* 2003). Towards the edges of the model volume the node spacing was increased to 50 km, with the outermost nodes removed by 300 km. The vertical node spacing similarly reflects the ray density, the spacing increasing with depth. The model consists of nine horizontal nodal layers, each layer comprising 31×25 nodes $= 775$ nodes. Nodes are only perturbed during inversion if more than five teleseismic rays pass in their vicinity. Initial velocity values were ascribed in accordance with accepted 1-D crustal and upper-mantle models (Landes *et al.* 2005; Kennett & Engdahl 1991) extrapolated to produce 3-D laterally homogeneous models. From this set an optimum laterally homogeneous starting model was selected based on extensive testing of combinations of velocity values, permitted standard deviations and nodal layer depths (O'Donnell 2010) (Table 1). Because we are inverting relative arrival time residuals, we can only infer relative velocity anomalies (similar considerations apply to the density anomalies). Consequently, the absolute 1-D earth starting velocity model values are of secondary importance to intra-layer lateral velocity model differences. Thus, in extrapolating from generic 1-D absolute starting velocity models to a 3-D laterally homogeneous starting model, we are in effect utilizing an unbiased model as our starting point.

Because the joint inversion algorithm requires a density layer corresponding to each velocity nodal plane, the density model similarly comprises nine layers extending to an overall depth of 320 km (Table 1). After testing a large range of block sizes to account for possible parametrization artefacts, lateral block dimensions varying between 30 and 70 km, and increasing with depth, were selected. As in the velocity model, each density layer incorporates large edge effect absorbing blocks extending beyond the data coverage area, again not represented in the final density model. Initial density values were ascribed in accordance with commonly accepted 1-D crustal and upper-mantle models (Dziewonski & Anderson 1981), again extrapolated to produce a 3-D laterally homogeneous starting model (Table 1).

4.4.1 Regularization

Apart from the first two layers of the velocity model, a uniform standard deviation of 0.2 km s^{-1} was assigned to all deeper layers, reflecting the lack of deep structural control. A similar constant standard deviation (0.3 km s^{-1}) was used by Tiberi *et al.* (2003) to account for a lack of *a priori* information in their study of the deep structure of the Baikal rift zone. The increased model parameter standard deviations assigned to the first two layers (0.4 and 0.3 km s^{-1}, respectively) were designed to reflect the pervasive lateral heterogeneity of Ireland's crust (e.g. Landes *et al.* 2005).

The density model standard deviations were chosen to reflect the information derived from the radially averaged power spectrum of the GRACE Bouguer anomaly (Fig. 5). Standard deviations are maximal for intermediate layer depths to encourage an appropriate depth emplacement of density contrasts. The smaller standard deviations for the shallowest and deepest layers reflect the fact that causative contrasts are not expected at those depths. The actual values of the density parameter standard deviations selected under this constraint are largely in line with values used in other studies (e.g. Tiberi *et al.* 2005; Basuyau *et al.* 2010).

Appropriate smoothing regularization was imposed based on the trade-off between root mean square (rms) data misfit reductions and the roughness of the anomaly structures, as advocated for studies such as this (e.g. Evans & Achauer 1993; Eberhart-Phillips 1986). Detailed trade-off curves are presented in the appendix which justify our choice of regularization values.

4.4.2 The B-coefficient

Although the algorithm envisages the B-coefficient as a parameter to be determined by the inversion, previous studies have alluded to the extreme non-linearity and instability introduced in allowing the B-coefficient to freely explore the parameter space (e.g. Tiberi *et al.* 2003; Basuyau *et al.* 2010). These authors found it necessary to limit the B-coefficient to a permitted range to produce geologically reasonable results. Through employing relatively low standard deviations in the variance matrix $\mathbf{C}_b$, we similarly constrain the B-coefficient such that it is not a truly free parameter to be inverted for. For mantle conditions, Birch (1961) determined a correlation coefficient of 3.05 km s^{-1} g^{-1} cm^3. Following this determination, an initial B-coefficient of 3 km s^{-1} g^{-1} cm^3 was assigned to all model layers (Table 1). A standard deviation of 0.05 km s^{-1} g^{-1} cm^3 was ascribed to the initial B-coefficients, in line with the $\sim$1 per cent standard error in determined B-coefficients as quoted by Birch (1961). This value neither over-imposes nor under-imposes the velocity–density relationship constraint (Appendix). Similar values were used by Tiberi *et al.* (2003) in their study of the Baikal rift zone and by Basuyau *et al.* (2010) in their study of the northern margin of the Gulf of Aden.

Table 1. The initial density and velocity model parametrizations for the joint inversion. Values are ascribed in accordance with commonly accepted crustal and upper-mantle values (e.g. Dziewonski & Anderson 1981; Kennett & Engdahl 1991; Landes *et al.* 2005). Corresponding model parameter standard deviations are shown in parentheses.

Layer	Depth (km)	Initial density (g cm^{-3})	Initial velocity (km s^{-1})	Initial B-coefficient (km s^{-1} g^{-1} cm^3)
1	0–10	2.67 (0.01)	6.00 (0.4)	3.00 (0.05)
2	10–25	2.75 (0.01)	6.80 (0.3)	3.00 (0.05)
3	25–50	2.90 (0.05)	8.00 (0.2)	3.00 (0.05)
4	50–80	3.30 (0.05)	8.08 (0.2)	3.00 (0.05)
5	80–110	3.38 (0.05)	8.15 (0.2)	3.00 (0.05)
6	110–150	3.38 (0.05)	8.18 (0.2)	3.00 (0.05)
7	150–190	3.38 (0.03)	8.20 (0.2)	3.00 (0.05)
8	190–250	3.38 (0.01)	8.60 (0.2)	3.00 (0.05)
9	250–320	3.43 (0.01)	8.70 (0.2)	3.00 (0.05)

5 RESOLUTION

The resolving power of the joint inversion scheme was assessed by examining its ability to retrieve standard synthetic checkerboard inputs where the parametrization, regularization and seismic source–receiver geometry are identical to that in the actual data inversion. The checkerboards consist of harmonically alternating high- and low-velocity anomalies with magnitudes $\delta V_P = \pm 10$ per cent, and corresponding density anomalies with magnitudes corresponding to B-coefficients of $3\,\mathrm{km\,s^{-1}\,g^{-1}\,cm^3}$. By using synthetic structure with similar length scales to the actual solution, reliable model regions can be inferred (e.g. Rawlinson & Sambridge 2003).

Fig. 7 shows input and retrieved models, including north–south and east–west oriented cross-sections, for a synthetic noise free checkerboard input at layer depth 50–80 km. The masked regions of the velocity model are regions of low ray density. As expected, the region of lateral velocity resolution for this depth largely reflects the areal extent of the seismic network, within which the velocity input is distinctively retrieved with only a small degree of lateral distortion. Laterally, the corresponding density checkerboard is well recovered. The effects of vertical smearing act to reduce the amplitudes of the recovered anomalies by approximately 75 per cent for the velocity model and by approximately 85 per cent for the density model. Amplitudes are, however, recovered most strongly at the input depth. Because short length-scale, steep gradient anomalies are penalized by our model regularization scheme, the checkerboard test does present pessimistic amplitude estimates. Longer wavelength resolution tests yield higher amplitude recovery than checkerboards (e.g. Bastow *et al.* 2005). Thus, employing checkerboards as a means of scaling between observed and actual amplitudes is unrobust. However, they are useful in highlighting reliable model regions.

Fig. 8 shows input and retrieved models for a checkerboard input at layer depth 250–320 km. The areal extent of the well-recovered region of the velocity input has increased at this depth due to the increased ray crossing. Again, only a small degree of lateral distortion in the pattern is evident. Velocity amplitude attenuation has also decreased slightly to approximately 65 per cent, with the amplitude again recovered most strongly at the input depth. As expected, the density model struggles to recover such a deep anomaly source. Any apparent coherent density recovery at this depth likely reflects the stronger velocity retrieval transmitted to the density model via the velocity–density link.

Taking a degree of vertical smearing into account, the checkerboard reconstructions show the joint inversion scheme to be capable of recovering lateral anomaly morphology to depths of ∼300 km. Furthermore, the reconstructions demonstrate the benefit of the joint inversion approach: at shallow depths, the strong density recovery complements the more limited velocity recovery, with the converse being true at greater depths.

6 RESULTS AND COMPARISON WITH OTHER STUDIES

Figs 9 and 10 show the velocity and density models retrieved by the joint inversion. After three iterations, the rms delay time data misfit was reduced from 0.19 to 0.12 s and the rms gravity data misfit from 38.61 to 1.07 mGal, corresponding to 35 and 97 per cent reductions, respectively. The final rms delay time data misfit of 0.12 s is ∼2.5 times the average MCCC estimated picking uncertainty. However, as previously stated, we regard the MCCC-derived estimates of picking uncertainty as optimistic. The final RMS gravity data misfit of 1.07 mGal compares with an estimated accumulated error in the GGM02C gravity model of about 1.5 mGal at degree 120 (wavelength ∼330 km) and 5 mGal at degree 200 (wavelength ∼200 km). It therefore falls within the estimated observational uncertainty.

Recovered velocity and density contrasts fall broadly within the ranges ±1.0 per cent and $\pm 0.03\,\mathrm{g\,cm^{-3}}$, respectively, the velocity amplitude range in line with that determined by Wawerzinek *et al.* (2008) in their tomographic study of Ireland's uppermost mantle *P*-wave velocity structure. However, the synthetic reconstructions have demonstrated that these values are almost certainly underestimated, and must therefore be treated tentatively.

The large-scale anomaly morphology we image generally correlates with the Wawerzinek *et al.* (2008) velocity model. At crustal depths, our velocity model is characterized by an abrupt change from high to low velocity contrast (∼ +1.5 to −1.5 per cent) across the southwest and the southern midlands of Ireland. The weak density anomalies imaged in the first two layers (0–25 km) likely result from vertical smearing, given that the anomaly morphology there reflects that imaged strongly at intermediate depths. The correlation between the velocity and density models for these layers is poor as expected, reflecting the lack of seismic resolution at these depths and the fact that long wavelength density anomalies are not expected there following the source depth estimates from the radially averaged power spectrum (Fig. 5).

Increased seismic resolution at depth slices 40, 60 and 85 km reveal a SW–NE trending low-velocity region across southern Ireland which branches northward across central Ireland. This is bounded to the east and west by high velocity anomalies. Correspondingly, three long wavelength low-density anomalies are imaged strongly between depths 25–80 km in southwest, southeast and west-northwest Ireland. At these depths, the velocity and density anomalies exhibit a clear correlation, demonstrating both the potential of GRACE data to probe upper-mantle structure and the apparent applicability of Birch's law to the subcrustal Irish lithosphere.

Offshore northwest Ireland, a longer wavelength SW–NE trending transition between low- and high-density contrasts is imaged, likely reflecting the continental slope of the Irish Atlantic margin. The high-density contrast reaches approximately $0.06\,\mathrm{g\,cm^{-3}}$ between depths 25–80 km. However, because of the lack of seismic resolution for this offshore region, no correlation between the models can be inferred. Beyond 80 km depth no significant density structure is imaged, in accordance with the source depth estimates from the radially averaged power spectrum (Fig. 5). As expected, we must rely on the seismic data to infer the uppermost mantle structure for these depths.

Velocity depth slices at 120 and 165 km reveal a NW–SE trending high-velocity zone beginning to dominate central Ireland in place of the adjacent low-velocity zone, which has migrated northeastward. Wawerzinek *et al.* (2008) similarly witness this transition at layer depth 120–150 km, but dismiss this structure as artefact based on their reconstruction tests, and as such offer a tectonic interpretation to 120 km depth only. Our reconstruction tests, however, indicate coherent structure retrieval at these depths. Furthermore, that the anomaly structure imaged by Wawerzinek *et al.* (2008) at layer depth 120–150 km correlates with that imaged in the our velocity models at depths 120 and 165 km lends weight to the contention that the structure is in fact not artefact.

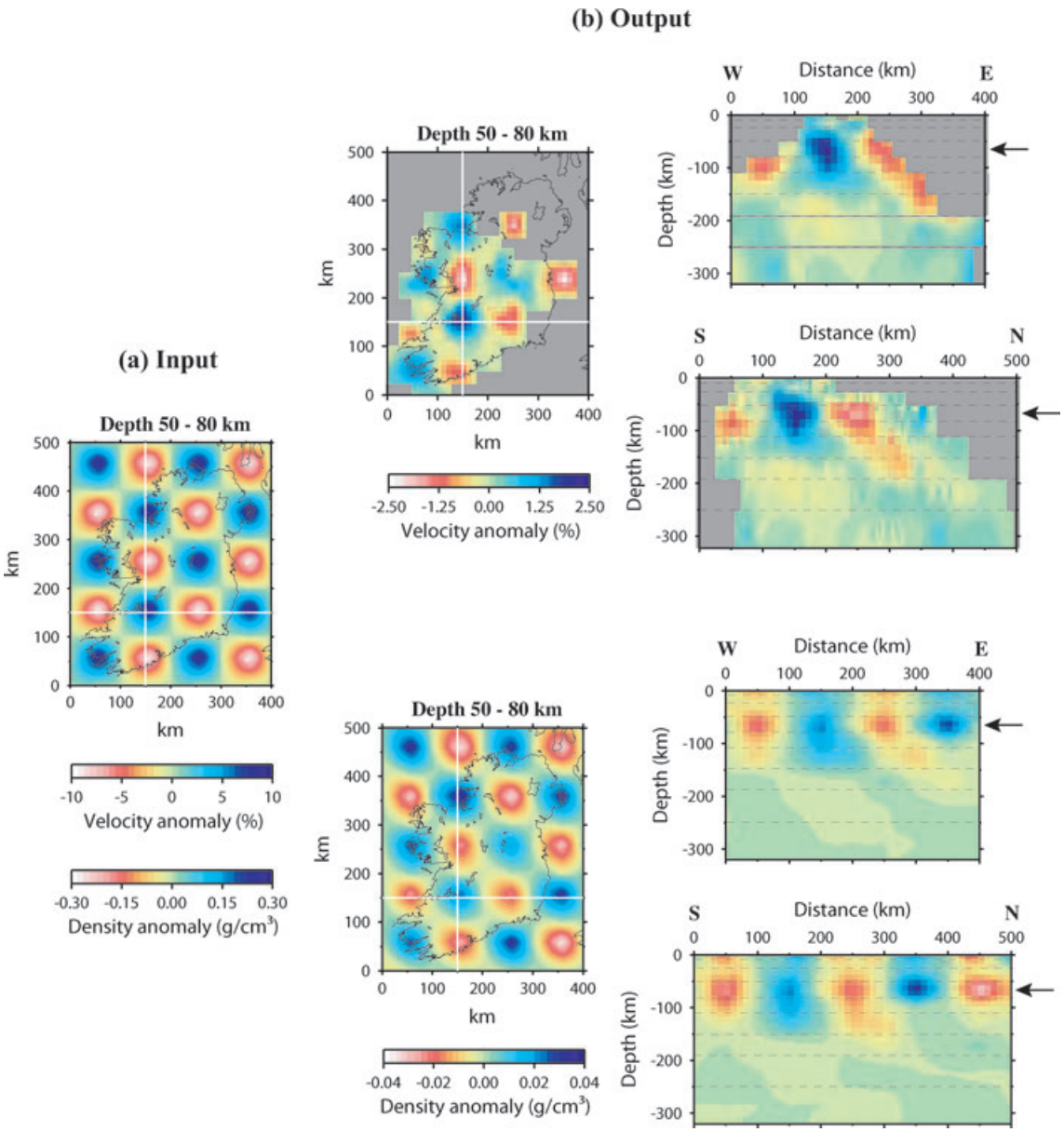

Figure 7. (a) Synthetic checkerboard anomaly input at layer depth 50–80 km. Anomalies are of wavelength 50 km with magnitudes $\delta V_P = \pm 10$ per cent and $\delta\rho = \pm 0.27$ g cm^{-3}, respectively. The white lines indicate the locations of the cross-sections. (b) The recovered velocity and density models with cross-sections. The masked regions are those where velocity nodes have not been inverted due to a low density of teleseismic rays. The black arrows on the cross-sections indicate the initial input depth of the synthetic anomalies.

Our array aperture allows us image the continued northeastward migration and broadening of the NW–SE trending high-velocity zone across central Ireland with depth, as revealed in the 220 and 285 km depth slices. It remains bound to the east and west by low-velocity zones, with a strong low-velocity contrast ($\delta V_P \sim -1$ per cent) imaged in northeast Ireland at depths 220 and 285 km. A tenuous correlation is inferred between this low-velocity contrast in northeast Ireland and a similar anomaly imaged in this region at approximately 200 km depth by Arrowsmith *et al.* (2005) in a *P*-wave tomographic study of uppermost mantle velocity structure beneath the British Isles. Otherwise, their synthetic reconstruction tests indicated that for depths shallower than 233 km, the region of credible resolution did not extend beyond the extreme east coast of Ireland, rendering a comparison with our models unfeasible.

7 DISCUSSION

7.1 Causes of mantle heterogeneity

Determining the causes of mantle heterogeneity in the Earth is not straightforward because a number of factors can affect density and seismic velocity, including temperature, partial melt and composition (e.g. Sobolev *et al.* 1996; Karato & Karki 2001). In addition, part of seismic velocity anomalies may reflect seismic anisotropy.

Temperature is often cited as the main source of mantle heterogeneity, but δV_P–T relationships can vary greatly depending on seismic attenuation (Q) (e.g. Karato 1993; Goes & van der Lee 2002). Constraints on Q for Ireland are lacking, but following Goes *et al.* (2000), a 100 °C increase in temperature could be associated with a decrease of 0.5–2 per cent in δV_P, taking

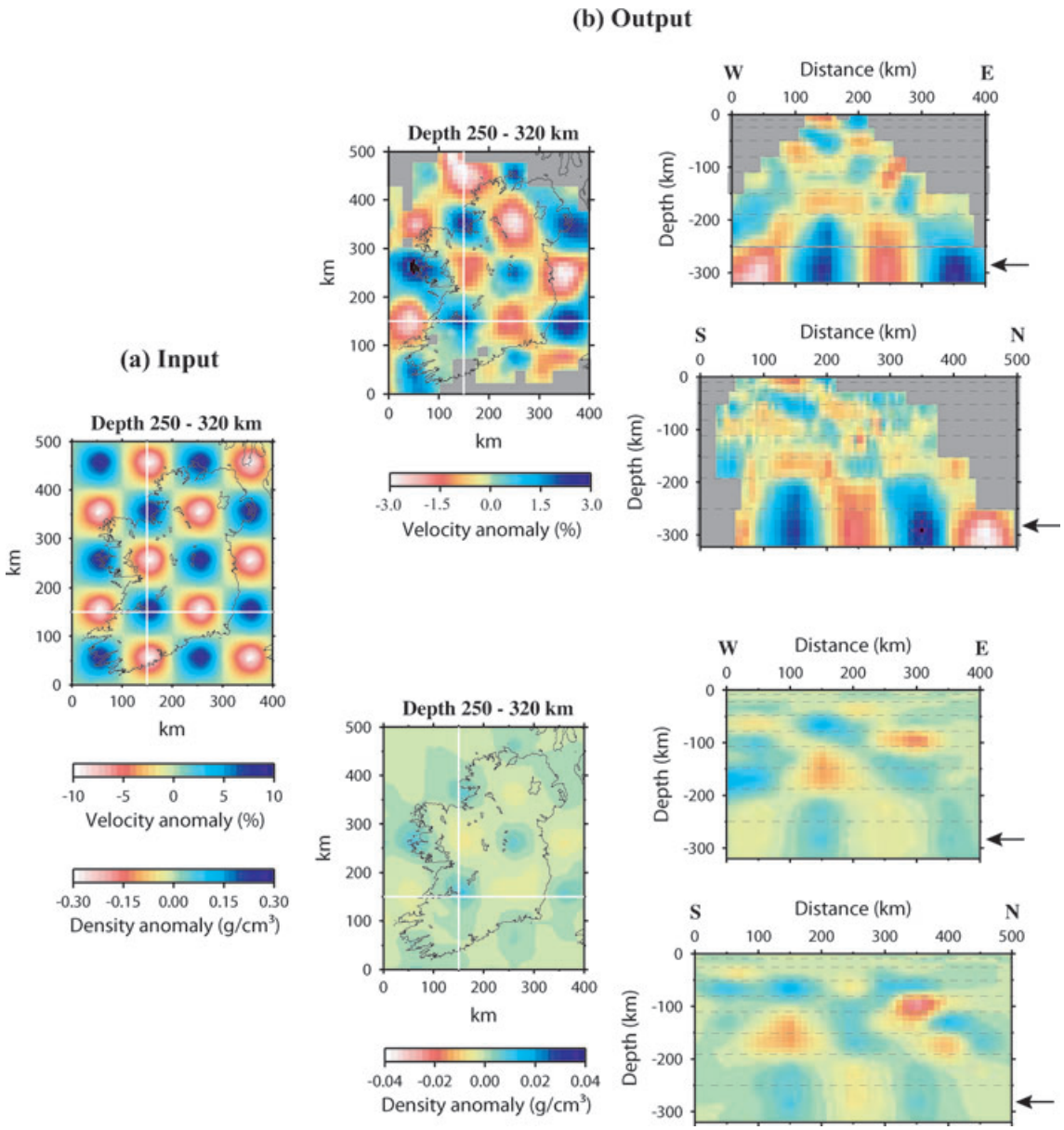

Figure 8. (a) Synthetic checkerboard anomaly input at layer depth 250–320 km. Anomalies are of wavelength 50 km with magnitudes $\delta V_P = \pm 10$ per cent and $\delta\rho = \pm 0.27$ g cm^{-3}, respectively. The white lines indicate the locations of the cross-sections. (b) The recovered velocity and density models with cross-sections. The masked regions are those where velocity nodes have not been inverted due to a low density of teleseismic rays. The black arrows on the cross-sections indicate the initial input depth of the synthetic anomalies.

account of both anelastic and anharmonic effects. Thus, the observed maximum peak-to-peak amplitudes of $\delta V_P < 1$ per cent we recover in the mantle (Fig. 9) could, if attributed solely to temperature effects, translate to lateral temperature variations of <50–200 °C. Similarly, assuming a linear $\delta\rho$–T relationship and a bulk expansion coefficient of 2.5×10^{-5} °C^{-1} for the upper mantle (e.g. Roy *et al.* 2005), the lateral density variations of $\delta\rho = \sim -0.03$ g cm^{-3} (about a reference value of 2.90 g cm^{-3}) imaged at 25–50 km depth (Fig. 10) could, if attributed solely to temperature variations, be explained by a thermal anomaly of ∼400°C.

However, when interpreting the results of tomographic studies such as this, it is important to bear in mind that relative arrival time residuals remove the mean velocity structure of a region (e.g. Bastow *et al.* 2005, 2008). In the case of Ireland, absolute *P*-wave delay times are fast compared to the global average (e.g. Poupinet 1979; Poupinet *et al.* 2003; Amaru *et al.* 2008) with the implication that low velocities presented in this study are not necessarily particularly slow compared to 'normal' mantle. In addition, global tomographic studies (e.g. Megnin & Romanowicz 2000; Montelli *et al.* 2006; Li *et al.* 2008) and regional surface-wave studies (e.g. Pilidou *et al.* 2004, 2005) indicate that fast *P*- and *S*-wave velocity anomalies characterize the mantle beneath Ireland and surrounding areas. Similar considerations apply in the case of the Bouguer anomaly. Although a Bouguer slab density of 2670 kg m^{-3} is most appropriate for Ireland (e.g. Armstrong 1997), the gross simplification leads to a degree of uncertainty in the background Bouguer anomaly value. This is particularly important when the anomalies are close to zero, as they are here (Fig. 4). In this case, relative anomaly contrasts can be more rigorously interpreted than the absolute anomaly values. Consequently, anomaly ratios based

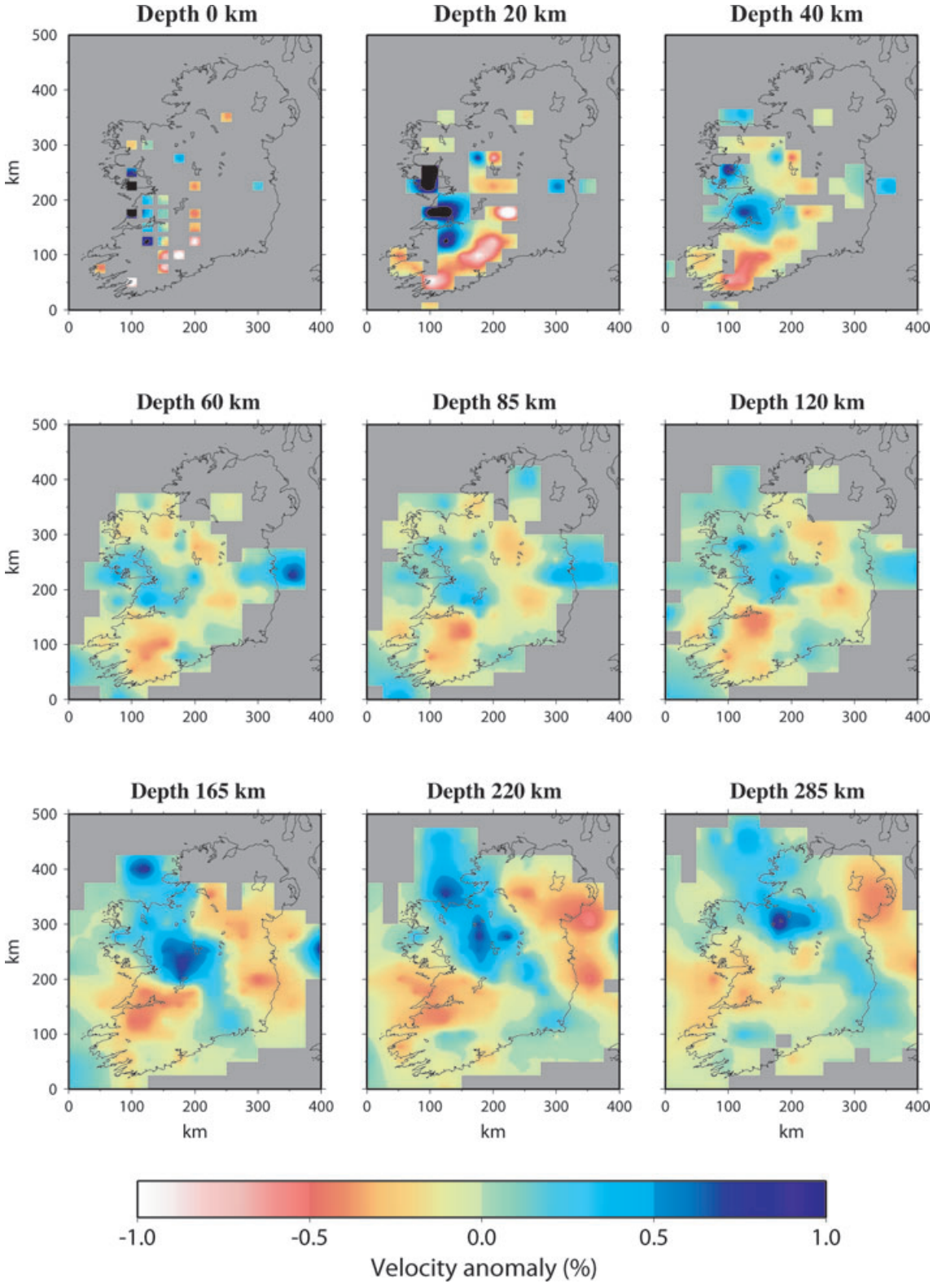

Figure 9. The joint inversion *P*-wave velocity model.

on the velocity and density models cannot be used as a means of elucidating possible heterogeneity sources due to the unknown background values.

Partial melt can have a strong effect on δV_P (e.g. 1 per cent melt can produce a -3.6 per cent δV_P anomaly; Hammond & Humphreys 2000). Furthermore, these effects are strongly dependent on melt geometry, which can enhance the impact on δV_P (e.g. Mavko 1980; Takei 2002). The amplitudes of velocity heterogeneities we observe beneath Ireland (although likely under estimated during the regularized inversion procedure) are, however, relatively low

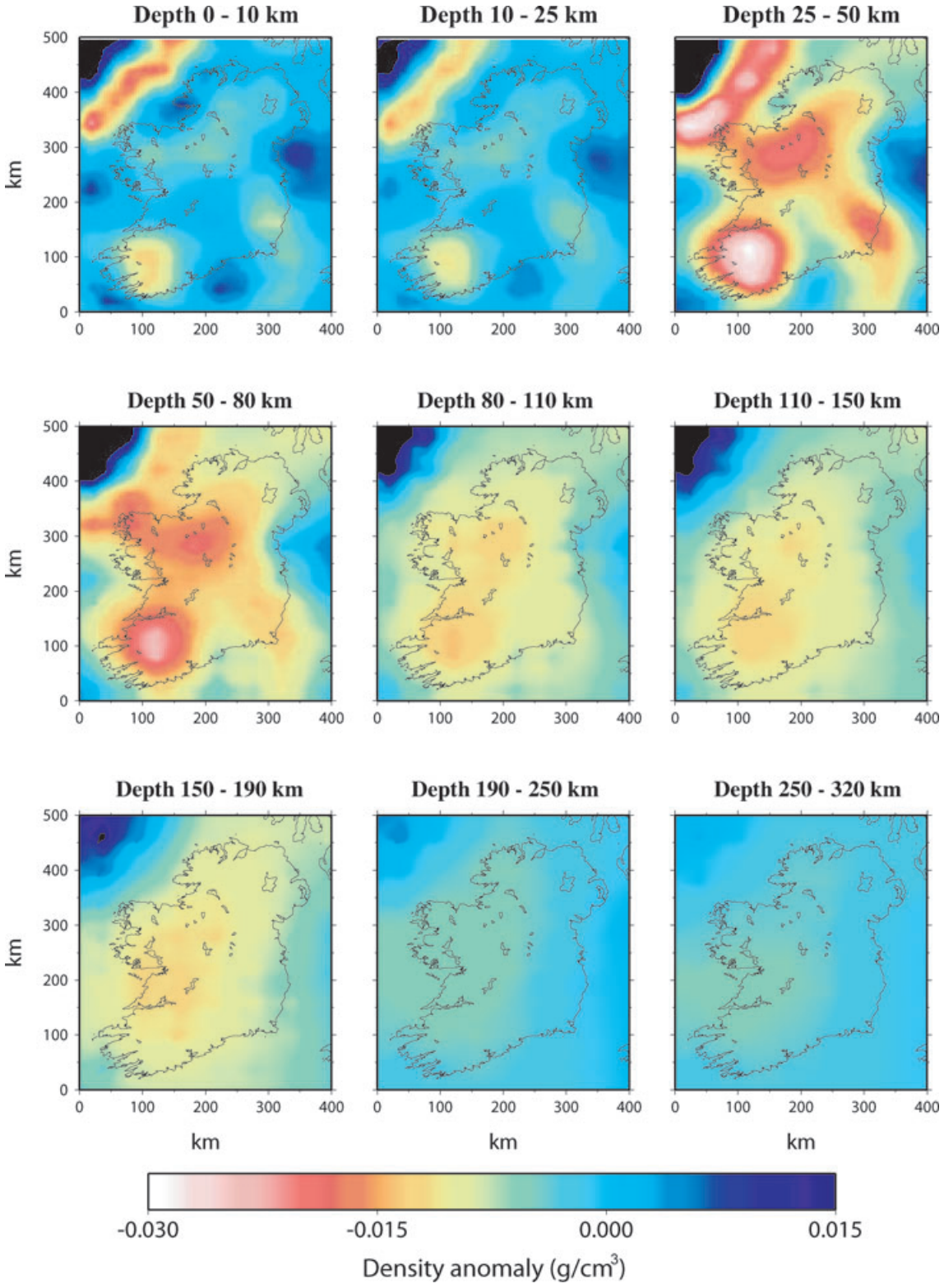

Figure 10. The joint inversion density model.

compared to those expected in the presence of partial melt. In any case, a thermally driven partial melt hypothesis for Ireland seems unlikely given the observation of relatively early absolute traveltimes and the evidence from the global and regional seismic literature.

Measurements of SKS shear-wave splitting in the region show that seismic anisotropic fabrics mirror Caledonian lithospheric trends and can be explained well by a single, horizontal layer of anisotropy (Helffrich 1995; Restivo & Helffrich 1999; Do *et al.* 2006; Bastow *et al.* 2007). Because the *P*-wave ray paths in

this study are almost perpendicular to these fabrics, our relative arrival time residuals should be largely unaffected by the effects of anisotropy. The absence of significant Caledonian trends in our velocity and density models (Figs 9 and 10) attests this.

Although temperature is often considered the principal cause of upper-mantle heterogeneity (e.g. Goes *et al.* 2000), some workers consider that composition can play a significantly stronger role. For example, a 100 °C anomaly can perhaps correspond to a $\delta V_P =$ 2–4 per cent anomaly of compositional origin (e.g. Deschamps *et al.* 2002; Artemieva *et al.* 2004). When considered in light of relatively early absolute traveltimes in Ireland and the surrounding British Isles, we suggest that the mantle heterogeneities we image are likely compositional in origin. In the following sections we explore this hypothesis in light of geodynamic constraints and evidence from the geological record.

7.2 The role of the Iceland Plume

Preceding studies of Irish and nearby British uppermost mantle velocity structure interpret low-velocity zones as regions of hot, partially molten Iceland plume material beneath regions of thinned lithosphere (Arrowsmith *et al.* 2005; Wawerzinek *et al.* 2008). Notably, the inferred magnitudes of the thermal seismic anomalies beneath Ireland (100–180°C; Wawerzinek *et al.* 2008) and Britain/Ireland (∼200°C; Arrowsmith *et al.* 2005) closely match those derived from seismic and geochemical studies in Iceland (e.g. 140–260 °C; Allen *et al.* 2002, and references therein). This is despite the observation that, in contrast to Ireland, *P*-wave delays at Iceland are among the slowest worldwide (e.g. Poupinet 1979) and upper-mantle seismic velocities beneath Ireland and Britain as illuminated by global and regional seismic studies (e.g. Megnin & Romanowicz 2000; Montelli *et al.* 2006; Li *et al.* 2008; Pilidou *et al.* 2004, 2005) are fast, not slow compared to the global average. The ponded plume hypothesis is also at odds with heat flow measurements from the same areas: Ireland—52–87 $\mathrm{mWm^{-1}}$ (Brock 1989; Armstrong 1997); Britain—$54 \pm 12\ \mathrm{mWm^{-1}}$ (e.g. Lee *et al.* 1987) and Iceland—100–300 $\mathrm{mWm^{-1}}$ (Flóvenz & Saemundsson 1993). We therefore seek an alternative explanation for the observed anomalies.

7.3 Lithosphere or asthenosphere?

Interpretation of our images is strongly dependent on assumptions of the depth of the LAB beneath Ireland. On the one hand, Landes *et al.* (2007) used *S*-to-*P* receiver functions to estimate a northward shallowing of the LAB from ∼85 to ∼55 km depth beneath central Ireland, purportedly the result of thermal erosion of the lower lithosphere by proto-Iceland plume material. The low-velocity and density heterogeneities we observe at depths greater than ∼50 km (Figs 9 and 10) would, in this instance, be interpreted as proto-Iceland plume material that has cooled since its emplacement during the break-up of Pangaea (∼60 Ma) and now forms a compositional anomaly compared to the Caledonian Irish lithosphere that surrounds it.

However, we calculate that the modelled lithospheric thinning would have generated at least 2 km of topography across the north of Ireland, a result difficult to reconcile with the uneroded Mesozoic to Cenozoic sequence of clastic shallow marine and lacustrine sediments observed in the northeast of Ireland (Simms 2009; Preston 2009). In light of this, we suggest that the southward dipping reflector interpreted by Landes *et al.* (2007) as the LAB may be one (or maybe more) of a series of regional southward dipping lithospheric mantle reflectors. Examples include the south–southwest dipping W reflector imaged at 10–20 km beneath the Moho offshore north of Scotland (Asencio *et al.* 2003, and references within) and the southward dipping crustal and upper lithospheric reflector seen on the SWAT 4 seismic reflection profile offshore southern Ireland (e.g. Klemperer & Hobbs 1991).

A much deeper 110–190 km LAB beneath Ireland was estimated by Clark & Stuart (1981) in a surface-wave study, a result reasonably consistent with an estimated depth of 130–150 km derived from a thermal model of the European lithosphere that uses the 1200°C isotherm as a proxy for LAB depth (Tesauro *et al.* 2009). In this instance, our images at 50–120 km depth would be explained better by intrinsic lithospheric compositional contrasts.

Masson *et al.* (1999) cited evidence from the traveltimes of *P* waves from a distant earthquake and Chinese nuclear test to suggest that the Paleozoic Iapetus suture in southwest Ireland is characterized by a marked change in lithospheric velocity structure. Our models support this hypothesis because they illuminate an abrupt increase in velocity and density northwards across the Shannon Estuary (Figs 1, 9 and 10). However, correlations between our imaged anomalies and the Iapetus suture are not apparent elsewhere in Ireland. Given that shear-wave splitting results have shown the lithosphere to be capable of preserving fossil anisotropic signatures over hundreds of millions of years (e.g. Helffrich 1995; Restivo & Helffrich 1999; Do *et al.* 2006; Bastow *et al.* 2007), the anomalies may reflect more complex accretionary growth associated with the Iapetus Ocean closure. A second possibility is that the anomalies reflect frozen decompressional melt which resulted from lithospheric thinning associated with the opening of the north Atlantic Ocean. A third possibility is that the anomalies reflect frozen plume related magmatic intrusions within the lithosphere, for which there is widespread support in the vicinity of the Irish Atlantic margin (e.g. Brodie & White 1994; Hall & White 1994; Al-Kindi *et al.* 2003; Tiley *et al.* 2004). However, given the lack of clear and consistent constraints on the deep basement of the Irish continental mass, these inferences are tentative.

7.4 Compositional variations and small-scale convection

Independent of assumptions of LAB depth, at depths greater than ∼120 km seismic heterogeneities cannot be explained easily in terms of lithospheric compositional contrasts, but the processes that cause them must be able to account for the continuation of anomalies across the LAB. To this end, we explore the process of sub-lithospheric small-scale convection, a phenomenon which can develop from the potential instability created by cold, dense mantle lithosphere overlying hotter, lighter, asthenosphere (e.g. Richter & Parsons 1975). If instabilities grow on timescales shorter than for which they can be erased by thermal diffusion, convective downwelling of the lower part of the lithosphere can result (Conrad & Molnar 1997).

From numerical simulations of 2-D convection cell growth, Dumoulin *et al.* (2005) determined an onset time for small-scale instabilities varying from 12–17 to 102–147 Myr, whereas Conrad & Molnar (1997) determined the wavelengths at which instabilities grow most rapidly for realistic continental lithospheric structures to be between 100 and 200 km. Houseman & Molnar (1997) cited the thermal diffusion timescale for perturbations of wavelengths 150 km as being about 20 Myr. Given that our velocity model exhibits anomalies at LAB depths of broadly comparable wavelengths

to those mentioned, we suggest that the respective timescales for instability growth and thermal diffusion reflect conditions permissible for the development of small-scale convective instabilities, particularly so in the presence of an early triggering mechanism, such as intrinsic lithospheric compositional variability (e.g. Elkins-Tanton 2005). Indeed, Elkins-Tanton & Hager (2000) contend that the intrusion and freezing of a small amount of melt within the mantle lithosphere acted as a triggering mechanism for sub-lithospheric small-scale convection in Siberia ∼250 Ma, with subsequent delamination leading to the eruption of the Siberian flood basalts.

We suggest that the lithospheric compositional contrasts alluded to may have triggered instability development at the base of the Irish lithosphere. Importantly, Conrad & Molnar (1997) determined that instabilities of plausible wavelength (100–200 km) beneath continents would not be expected to produce measurable surface deformation, consistent with what is observed in this tectonically inactive low-lying region. Furthermore, following the findings of Marquart & Schmeling (1989), small-scale convection related free air gravity anomalies of less than ∼20 mGal would be predicted over Ireland, broadly in line with the observed GRACE GGM02C free air gravity anomaly (Fig. 4).

8 CONCLUSION

By jointly inverting teleseismic *P*-wave delay times with the long wavelength GRACE gravity anomaly in Ireland, we address a disconnect that exists in the literature between a lithosphere pervaded by Palaeozoic signatures and an asthenosphere purportedly dominated by Tertiary structure. We argue that the anomalies imaged at lithospheric depths must reflect compositional, rather than plume-driven thermal contrasts, either due to terrane accretion associated with Iapetus Ocean closure, frozen decompressional melt generated during the opening of the north Atlantic Ocean, frozen Iceland plume related magmatic intrusions, or a combination thereof. To explain the continuation of the anomalous structure into the asthenosphere, we suggest that the lithospheric compositional contrasts may have initiated small-scale convection at the base of the lithosphere. Our coherent velocity and density uppermost mantle models thus demonstrate that Tertiary asthenospheric structure is likely intimately related to (possibly ancient) lithospheric structure.

ACKNOWLEDGMENTS

The authors thank Richard W. England, Paul D. Ryan and Martin Feely for their input into this project. Constructive comments from editor Saskia Goes and two anonymous reviewers improved the paper. The seismic data were collected during the ISLE and ISUME projects undertaken by the Dublin Institute for Advanced Studies. ISLE was funded by an Enterprise Ireland Basic Research Grant SC/01/155 and ISUME is funded by a Science Foundation Ireland research Frontiers Programme Grant GEO758. This project was funded by a National University of Ireland, Galway (NUIG) postgraduate fellowship and the IRCSET Ulysses initiative. Figures in the paper were produced using the Generic Mapping Tools (GMT) software package of Wessel & Smith (1998).

REFERENCES

Al-Kindi, S., White, N., Sinha, M., England, R. & Tiley, R., 2003. Crustal trace of a hot convective sheet, *Geology,* **31**(3), 207–210.

Allen, R.M. *et al.,* 2002. Imaging the mantle beneath Iceland using integrated seismological techniques, *J. geophys. Res.,* **107**(B12), 2325, doi:10.1029/2001JB000595.

Amaru, M.L., Spakman, W., Villaseñor, A., Sandoval, S. & Kissling, E., 2008. A new absolute arrival time data set for Europe, *Geophys. J. Int.,* **173,** 465–472.

Armstrong, G.D., 1997. Potential field signatures and flexural rigidity of the lithosphere in Ireland, *PhD thesis,* Applied Geophysics Unit, University College Galway, Ireland.

Arrowsmith, S.J., Kendall, M., White, N., VanDecar, J.C. & Booth, D.C., 2005. Seismic imaging of a hot upwelling beneath the British Isles, *Geology,* **33**(5), 345–348.

Artemieva, I.M., Billien, M., Leveque, J.J. & Mooney, W.D., 2004. Shear wave velocity, seismic attenuation, and thermal structure of the continental upper mantle, *Geophys. J. Int.,* **157,** 607–628.

Asencio, E., Knapp, J.H., Owens, T.J. & Helffrich, G., 2003. Mapping fine-scale heterogeneities within the continental mantle lithosphere beneath Scotland: combining active- and passive-source seismology, *Geology,* **31**(6), 477–480.

Barrat, J.A. & Nesbitt, R.W., 1996. Geochemistry of the Tertiary volcanism of Northern Ireland, *Chem. Geol.,* **129,** 15–38.

Barton, P.J., 1992. LISPB revisited: a new look under the Caledonides of northern Britain, *Geophys. J. Int.,* **110**(2), 371–391.

Bastow, I.D., Stuart, G.W., Kendall, J.M. & Ebinger, C.J., 2005. Upper-mantle seismic structure in a region of incipient continental breakup: northern Ethiopian Rift, *Geophys. J. Int.,* **162,** 479–493.

Bastow, I.D., Owens, T.J., Helffrich, G. & Knapp, J.H., 2007. Spatial and temporal constraints on sources of seismic anisotropy: evidence from the Scottish highlands, *Geophys. Res. Lett.,* **34,** L05303, doi:10.1029/2006GL028911.

Bastow, I.D., Nyblade, A.A., Stuart, G.W., Rooney, T.O. & Benoit, M.H., 2008. Upper mantle seismic structure beneath the Ethiopian hot spot: rifting at the edge of the African low-velocity anomaly, *Geochem. Geophys. Geosyst.,* **9**(12), Q12022, doi:10.1029/2008GC002107.

Basuyau, C., Tiberi, C., Leroy, S., Stuart, G., Al-Lazki, A., Al-Toubi, K. & Ebinger, C., 2010. Evidence of partial melting beneath a continental margin: case of Dhofar, in the Northeast Gulf of Aden (Sultanate of Oman), *Geophys. J. Int.,* **180**(2), 520–534.

Birch, F., 1961. The velocity of compressional waves in rocks to 10 kilobars, part 2, *J. geophys. Res.,* **66**(7), 2199–2224.

Brock, A., 1989. Heat flow measurements in Ireland, *Tectonophysics,* **164**(2–4), 231–236.

Brodie, J. & White, N., 1994. Sedimentary basin inversion caused by igneous underplating: Northwest European continental shelf, *Geology,* **22,** 147–150.

Chadwick, R.A. & Pharaoh, T.C., 1998. The seismic reflection Moho beneath the United Kingdom and adjacent areas, *Tectonophysics,* **299**(4), 255–279.

Christensen, N.I. & Mooney, W.D., 1995. Seismic velocity structure and composition of the continental crust: a global view, *J. geophys. Res.,* **100**(B6), 9761–9788.

Chung, D.H., 1972. Birch's Law: why is it so good? *Science,* **177**(4045), 261–263.

Clark, R.A. & Stuart, G.W., 1981. Upper mantle structure of the British Isles from Rayleigh wave dispersion, *Geophys. J. R. astr. Soc.,* **67,** 59–75.

Conrad, C.P. & Molnar, P., 1997. The growth of Rayleigh-Taylor-type instabilities in the lithosphere for various rheological and density structures, *Geophys. J. Int.,* **129,** 95–112.

Cooper, M.A., Collins, D.A., Ford, M., Murphy, F.X., Trayner, P.M. & O'Sullivan, M., 1986. Structural evolution of the Irish Variscides, *J. geol. Soc. Lond.,* **143**(1), 53–61.

Daly, E., Brown, C., Stark, C.P. & Ebinger, C.J., 2004. Wavelet and multitaper coherence methods for assessing the elastic thickness of the Irish Atlantic margin, *Geophys. J. Int.,* **159**(2), 445–459.

Deschamps, F., Trampert, J. & Snieder, R., 2002. Anomalies of temperature and iron in the uppermost mantle inferred from gravity data and tomographic models, *Phys. Earth planet. Int.,* **129,** 245–264.

Di Leo, J., Bastow, I.D. & Helffrich, G., 2009. Nature of the Moho beneath the Scottish Highlands from a receiver function perspective, *Tectonophysics,* **479**(3–4), 214–222.

Do, V.C., Readman, P.W., O'Reilly, B.M. & Landes, M., 2006. Shear-wave splitting observations across southwest Ireland, *Geophys. Res. Lett.,* **33,** L03309, doi:10.1029/2005GL024496.

Dumoulin, C., Doin, M.P., Arcay, D. & Fleitout, L., 2005. Onset of small-scale instabilities at the base of the lithosphere: scaling laws and role of pre-existing lithospheric structures, *Geophys. J. Int.,* **160,** 344–356.

Dziewonski, A.M. & Anderson, D.L., 1981. Preliminary reference Earth model, *Phys. Earth planet. Int.,* **25**(4), 297–356.

Eberhart-Phillips, D., 1986. Three-dimensional velocity structure in northern California Coast Ranges from inversion of local earthquake arrival times, *Bull. seism. Soc. Am.,* **76**(4), 1025–1052.

Elkins-Tanton, L.T., 2005. Continental magmatism caused by lithospheric delamination, in *Plates, Plumes and Paradigms,* pp. 449–461, eds Foulger, G.R., Natland, J.H., Presnall, D.C. & Anderson, D.L., Geological Society of America, Special Paper 388.

Elkins-Tanton, L.T. & Hager, B.H., 2000. Melt intrusion as a trigger for lithospheric foundering and the eruption of the Siberian flood basalt, *Geophys. Res. Lett.,* **27**(23), 3937–3940.

Evans, J.R. & Achauer, U., 1993. Teleseismic velocity tomography using the ACH method: theory and application to continental-scale studies, in *Seismic Tomography: Theory and Practice,* eds Iyer, H.M. & Hirahara, K., Chapman & Hall, London.

Flóvenz, O. & Saemundsson, K., 1993. Heat flow and geothermal processes in Iceland, *Tectonophysics,* **225**(1–2), 123–138.

Ford, M., Brown, C. & Readman, P., 1991. Analysis and tectonic interpretation of gravity data over the Variscides of southwest Ireland, *J. geol. Soc. Lond.,* **148**(1), 137–148.

Gamble, J.A., Wysoczanski, R.J. & Meighan, I.G., 1999. Constraints on the age of the British Tertiary Volcanic Province from ion microprobe U-Pb (SHRIMP) ages for acid igneous rocks from NE Ireland, *J. geol. Soc. Lond.,* **156**(2), 291–299.

Gill, W.D., 1962. The Variscan fold belt in Ireland, in *Some Aspects of the Variscan Fold Belt,* pp. 49–64, ed. Coe, K., Manchester University Press, Manchester.

Goes, S. & van der Lee, S., 2002. Thermal structure of the North American uppermost mantle inferred from seismic tomography, *J. geophys. Res.,* **107**(B3), doi:10.1029/2000JB000049.

Goes, S., Govers, R. & Vacher, P., 2000. Shallow mantle temperatures under Europe from P and S wave tomography, *J. geophys. Res.,* **105**(B5), 11 153–11 169.

Grad, M., Tiira, T. & the ESC Working Group, 2009. The Moho depth map of the European Plate, *Geophys. J. Int.,* **176**(1), 279–292.

Haber, E. & Oldenburg, D., 1997. Joint inversion: a structural approach, *Inverse Probl.,* **13,** 63–77.

Hall, B.D. & White, N., 1994. Origin of anomalous Tertiary subsidence adjacent to North Atlantic continental margins, *Mar. Petrol. Geol.,* **11**(6), 702–714.

Hammond, W.C. & Humphreys, E.D., 2000. Upper mantle seismic wave velocity: effects of realistic partial melt geometries, *J. geophys. Res.,* **105**(B5), 10975–10986.

Hansen, S.E., Schwartz, A.J.R.S.Y. & Al-Amri, A.M.S., 2007. Imaging ruptured lithosphere beneath the Red Sea and Arabian Peninsula, *Earth planet. Sci. Lett.,* **259,** 256–265.

Hauser, F., O'Reilly, B.M., Readman, P.W., Daly, J.S. & Van den Berg, R., 2008. Constraints on crustal structure and composition within a continental suture zone in the Irish Caledonides from shear wave wide-angle reflection data and lower crustal xenoliths, *Geophys. J. Int.,* **175**(3), 1254–1272.

Heiskanen, W.A. & Moritz, H., 1967. *Physical Geodesy,* W.H. Freeman and Company, San Francisco.

Helffrich, G., 1995. Lithospheric deformation inferred from teleseismic shear wave splitting observations in the United Kingdom, *J. geophys. Res.,* **100**(B9), 18 195–18 204.

Houseman, G.A. & Molnar, P., 1997. Gravitational (Rayleigh-Taylor) instability of a layer with non-linear viscosity and convective thinning of continental lithosphere, *Geophys. J. Int.,* **128,** 125–150.

Jackson, D.D. & Matsu'ura, M., 1985. A Bayesian approach to nonlinear inversion, *J. geophys. Res.,* **90**(B1), 581–591.

Jacob, A.W.B., Kaminski, W., Murphy, T., Phillips, W.E.A. & Prodehl, C., 1985. A crustal model for a northeast-southwest profile through Ireland, *Tectonophysics,* **113,** 75–103.

Jordan, M., 2003. JI-3D A new approach to high resolution regional seismic tomography: theory and applications, *PhD thesis*, Georg-August-University Göttingen.

Karato, S., 1993. Importance of anelasticity in the interpretation of seismic tomography, *Geophys. Res. Lett.,* **20**(15), 1623–1626.

Karato, S. & Karki, B.B., 2001. Origin of lateral variation of seismic wave velocities and density in the deep mantle, *J. geophys. Res.,* **106**(B10), 21 771–21 783.

Kennett, B.L.N. & Engdahl, E.R., 1991. Traveltimes for global earthquake location and phase identification, *Geophys. J. Int.,* **105**(2), 429–465.

Kirstein, L.A. & Timmerman, M.J., 2000. Evidence of the proto-Iceland plume in northwestern Ireland at 42 Ma from helium isotopes, *J. geol. Soc. Lond.,* **157**(5), 923–928.

Klemperer, S. & Hobbs, R., 1991. *The BIRPS Atlas: Deep Seismic Reflection Profiles Around the British Isles,* Cambridge University Press, Cambridge.

Landes, M., Ritter, J.R.R., Readman, P.W. & O'Reilly, B.M., 2005. A review of the Irish crustal structure and signatures from the Caledonian and Variscan Orogenies, *Terra Nova,* **17**(2), 111–120.

Landes, M., Rittera, J.R.R. & Readman, P.W., 2007. Proto-Iceland plume caused thinning of Irish lithosphere, *Earth planet. Sci. Lett.,* **255,** 32–40.

Lee, M.K., Brown, G.C., Webb, P.C., Wheildon, J. & Rollin, K.E., 1987. Heat flow, heat production and thermo-tectonic setting in mainland UK, *J. geol. Soc. Lond.,* **144**(1), 35–42.

Lees, J.M. & VanDecar, J.C., 1991. Seismic tomography constrained by Bouguer gravity anomalies: applications in Western Washington, *Pure appl. Geophys.,* **135**(1), 31–52.

Lemoine, F.G. *et al.,* 1998. *The Development of the Joint NASA GSFC and NIMA Geopotential Model EGM96*, NASA/TP-1998-206861, NASA Goddard Space Flight Center, Greenbelt, Maryland, 20771 USA.

Li, C., van der Hilst, R.D., Engdahl, R. & Burdick, S., 2008. A new global model for P wave speed variations in Earth's mantle, *Geochem. Geophys. Geosyst.,* **9**(5), Q05018, doi:10.1029/2007GC001806.

Li, Y. & Oldenburg, D.W., 1998. 3-D inversion of gravity data, *Geophysics,* **63**(1), 109–119.

Lowe, C. & Jacob, A.W.B., 1989. A north-south seismic profile across the Caledonian suture zone in Ireland, *Tectonophysics,* **168**(4), 297–318.

Marquart, G. & Schmeling, H., 1989. Topography and geoid undulations caused by small-scale convection beneath continental lithosphere of variable elastic thickness, *Geophys. J.,* **97,** 511–527.

Masson, F., Hauser, F. & Jacob, A.W.B., 1999. The lithospheric trace of the Iapetus suture in SW Ireland from teleseismic data, *Tectonophysics,* **302,** 83–98.

Mavko, G.M., 1980. Velocity and attenuation in partially molten rocks, *J. geophys. Res.,* **85**(B10), 5173–5189.

Megnin, C. & Romanowicz, B., 2000. The three-dimensional shear velocity structure of the mantle from the inversion of body, surface and higher-mode waveforms, *Geophys. J. Int.,* **143**(3), 709–728.

Montelli, R., Nolet, G., Dahlen, F.A. & Masters, G., 2006. A catalogue of deep mantle plumes: new results from finite-frequency tomography, *Geochem. Geophys. Geosyst.,* **7,** Q11007, doi:10.1029/2006GC001248.

Moucha, R., Forte, A.M., Mitrovica, J.X., Rowley, D.B., Quéré, S., Simmons, N.A. & Grand, S.P., 2008. Dynamic topography and long-term sea-level variations: there is no such thing as a stable continental platform, *Earth planet. Sci. Lett.,* **271,** 101–108.

Mussett, A.E., Dagley, P. & Skelhorn, R.R., 1988. Time and duration of activity in the British Tertiary Igneous Province, in *Early Tertiary Volcanism and the Opening of the NE Atlantic,* Vol. 39, pp. 337–348, eds Morton, A.C. & Parson, L.M., Geological Society, London, Special Publications.

Naylor, D. & Shannon, P., 2009. The geology of offshore Ireland, in *The Geology of Ireland,* pp. 405–460, eds Holland, C.H. & Sanders, I.S., Dunedin Academic Press, Edinburgh.

O'Donnell, J., 2010. A gravity and teleseimic study of Ireland's crustal and upper mantle structure, *PhD thesis,* National University of Ireland, Galway.

O'Reilly, B.M., Readman, P.W. & Hauser, F., 1998. Lithospheric structure across the western Eurasian plate from a wide-angle seismic and gravity study: evidence for a regional thermal anomaly, *Earth planet. Sci. Lett.,* **156**(3–4), 275–280.

O'Reilly, B.M., Hauser, F. & Readman, P.W., 2010. The fine-scale structure of upper continental lithosphere from seismic waveform methods: insights into Phanerozoic crustal formation processes, *Geophys. J. Int.,* **180**(1), 101–124, doi: 10.1111/j.1365-246X.2009.04420.x.

Pawlowski, R.S., 1995. Preferential continuation for potential field anomaly enhancement, *Geophysics,* **60**(2), 390–398.

Phillips, W.E.A., Stillman, C.J. & Murphy, T., 1976. A Caledonian plate tectonic model, *J. geol. Soc. Lond.,* **132**(6), 579–605.

Pilidou, S., Priestley, K., Gudmundsson, O. & Debayle, E., 2004. Upper mantle S-wave speed heterogeneity and anisotropy beneath the North Atlantic from regional surface wave tomography: the Iceland and Azores plumes, *Geophys. J. Int.,* **159**(3), 1057–1076.

Pilidou, S., Priestley, K., Debayle, E. & Gudmundsson, O., 2005. Rayleigh wave tomography in the North Atlantic: high resolution images of the Iceland, Azores and Eifel mantle plumes, *Lithos,* **79**(3–4), 453–474.

Poupinet, G., 1979. On the relation between P-wave travel time residuals and the age of continental plates, *Earth planet. Sci. Lett.,* **43**(1), 149–161.

Poupinet, G., Arndt, N. & Vacher, P., 2003. Seismic tomography beneath stable tectonic regions and the origin and composition of the continental lithospheric mantle, *Earth planet. Sci. Lett.,* **212**(1–2), 89–101.

Preston, J., 2009. Tertiary igneous activity, in *The Geology of Ireland,* pp. 333–354, eds Holland, C.H. & Sanders, I.S., Dunedin Academic Press, Edinburgh.

Rao, C.K., Jones, A.G. & Moorkamp, M., 2007. The geometry of the Iapetus Suture Zone in central Ireland deduced from a magnetotelluric study, *Phys. Earth planet. Int.,* **161,** 134–141.

Rawlinson, N. & Sambridge, M., 2003. Seismic traveltime tomography of the crust and lithosphere, *Adv. Geophys.,* **46,** 81–197.

Readman, P.W., O'Reilly, B.M. & Murphy, T., 1997. Gravity gradients and upper-crustal tectonic fabrics, Ireland, *J. geol. Soc. Lond.,* **154**(5), 817–828.

Restivo, A. & Helffrich, G., 1999. Teleseismic shear wave splitting measurements in noisy environments, *Geophys. J. Int.,* **137,** 821–830.

Richter, F.M. & Parsons, B., 1975. On the interaction of two scales of convection in the mantle, *J. geophys. Res.,* **80**(17), 2529–2541.

Roy, M., MacCarthy, J.K. & Selverstone, J., 2005. Upper mantle structure beneath the eastern Colorado Plateau and Rio Grande rift revealed by Bouguer gravity, seismic velocities, and xenolith data, *Geochem. Geophys. Geosyst.,* **6,** Q10007, doi:10.1029/2005GC001008.

Shin, Y.H., Xu, H., Braitenberg, C., Fang, J. & Wang, Y., 2007. Moho undulations beneath Tibet from GRACE-integrated gravity data, *Geophys. J. Int.,* **170,** 971–985.

Shin, Y.H., Shum, C.K., Braitenberg, C., Lee, S.M., Xu, H., Choi, K.S., Baek, J.H. & Park, J.U., 2009. Three-dimensional fold structure of the Tibetan Moho from GRACE gravity data, *Geophys. Res. Lett.,* **36,** L01302, doi:10.1029/2008GL036068.

Simms, M.J., 2009. Permian and Mesozoic, in *The Geology of Ireland,* pp. 311–332, eds Holland, C.H. & Sanders, I.S., Dunedin Academic Press, Edinburgh.

Sobolev, S.V., Zeyen, H., Stoll, G., Werling, F., Altherr, R. & Fuchs, K., 1996. Upper mantle temperatures from teleseismic tomography of French Massif Central including effects of composition, mineral reactions, anharmonicity, anelasticity and partial melt, *Earth planet. Sci. Lett.,* **139,** 147–163.

Spector, A. & Grant, F.S., 1970. Statistical models for interpreting aeromagnetic data, *Geophysics,* **35**(2), 293–302.

Steck, L.K. & Prothero, W.A., 1991. A 3-D raytracer for teleseismic body-wave arrival times, *Bull. seism. Soc. Am.,* **81**(4), 1332–1339.

Takei, Y., 2002. Effect of pore geometry on V_p/V_s: from equilibrium geometry to crack, *J. geophys. Res.,* **107**(B2), doi:10.1029/2001JB000522.

Tapley, B. *et al.,* 2005. GGM02—an improved Earth gravity field model from GRACE, *J. Geod.,* **79**(8), 467–478.

Tesauro, M., Kaban, M.K., Cloetingh, S.A. P.L., Hardebol, N.J. & Beekman, F., 2007. 3D strength and gravity anomalies of the European lithosphere, *Earth planet. Sci. Lett.,* **263,** 56–73.

Tesauro, M., Kaban, M.K. & Cloetingh, S.A.P.L., 2009. A new thermal and rheological model of the European lithosphere, *Tectonophysics,* **476,** doi:10.1016/j.tecto.2009.07.022.

Thurber, C.H., 1983. Earthquake locations and three-dimensional crustal structure in the Coyote Lake area, Central California, *J. geophys. Res.,* **88**(B10), 8226–8236.

Tiberi, C., Diament, M., Déverchère, J., Petit-Mariani, C., Mikhailov, V., Tikhotsky, S. & Achauer, U., 2003. Deep structure of the Baikal rift zone revealed by joint inversion of gravity and seismology, *J. geophys. Res.,* **108**(B3), 2133, doi:10.1029/2002JB001880.

Tiberi, C., Ebinger, C., Ballu, V., Stuart, G. & Oluma, B., 2005. Inverse models of gravity data from the Red Sea-Aden-East African rifts triple junction zone, *Geophys. J. Int.,* **163**(2), 775–787.

Tiley, R., White, N. & Al-Kindi, S., 2004. Linking Paleogene denudation and magmatic underplating beneath the British Isles, *Geol. Mag.,* **141**(3), 345–351.

Tilmann, F.J., Benz, H.M., Priestley, K.F. & Okubo, P.G., 2001. P-wave velocity structure of the uppermost mantle beneath Hawaii from traveltime tomography, *Geophys. J. Int.,* **146**(3), 594–606.

Tomlinson, J.P., Denton, P., Maguire, P.K.H. & Booth, D.C., 2006. Analysis of the crustal velocity structure of the British Isles using teleseismic receiver functions, *Geophys. J. Int.,* **167**(1), 223–237.

VanDecar, J.C. & Crosson, R.S., 1990. Determination of teleseismic relative phase arrival times using multi-channel cross-correlation and least squares, *Bull. seism. Soc. Am.,* **80**(1), 150–169.

VanDecar, J.C., James, D.E. & Assumpcao, M., 1995. Seismic evidence for a fossil mantle plume beneath South America and implications for plate driving forces, *Nature,* **378,** 25–31.

Wawerzinek, B., Ritter, J.R.R., Jordan, M. & Landes, M., 2008. An upper-mantle upwelling underneath Ireland revealed from non-linear tomography, *Geophys. J. Int.,* **175**(1), 253–268.

Wessel, P. & Smith, W.H.F., 1998. New, improved version of the Generic Mapping Tools released, *EOS, Trans. Am. geophys. Un.,* **79,** 579.

White, R. & McKenzie, D., 1989. Magmatism at rift zones: the generation of volcanic continental margins and flood basalts, *J. geophys. Res.,* **94**(B6), 7685–7729.

White, R.S., Smith, L.K., Roberts, A.W., Christie, P.A.F., Kusznir, N.J., & the rest of the iSIMM Team, 2008. Lower-crustal intrusion on the North Atlantic continental margin, *Nature,* **452,** 460–464.

Woodcock, N.H. & Strachan, R.A., 2000. The Caledonian Orogeny: a multiple plate collision, in *Geological History of Britain and Ireland,* eds Woodcock, N.H. & Strachan, R.A., Blackwell Science, Oxford.

Zeyen, H. & Achauer, U., 1997. Joint inversion of teleseismic delay times and gravity anomaly data for regional structures: theory and synthetic examples, in *Upper Mantle Heterogeneities from Active and Passive Seismology,* Proceedings of the NATO Advanced Research Workshop, Moscow, Russia, 1997 April 13–16, pp. 155–168, ed. Fuchs, K., Kluwer Academic Publishers, Dordrecht.

APPENDIX: REGULARIZATION

The respective influence of each of the regularization terms on the joint inversion is demonstrated through Figs A1–A3.

Fig. A1 illustrates the trade-off between velocity model roughness and seismic data fitting in the joint inversion as a function of velocity model parameter standard deviations. A standard deviation of $0.2\,\mathrm{km\,s^{-1}}$ was selected from the 'knee' of the trade-off curve as appropriate for the inversion. Beyond this standard deviation value, the data fit remains almost stationary, but the model roughness continues to increase, likely indicating spurious structure.

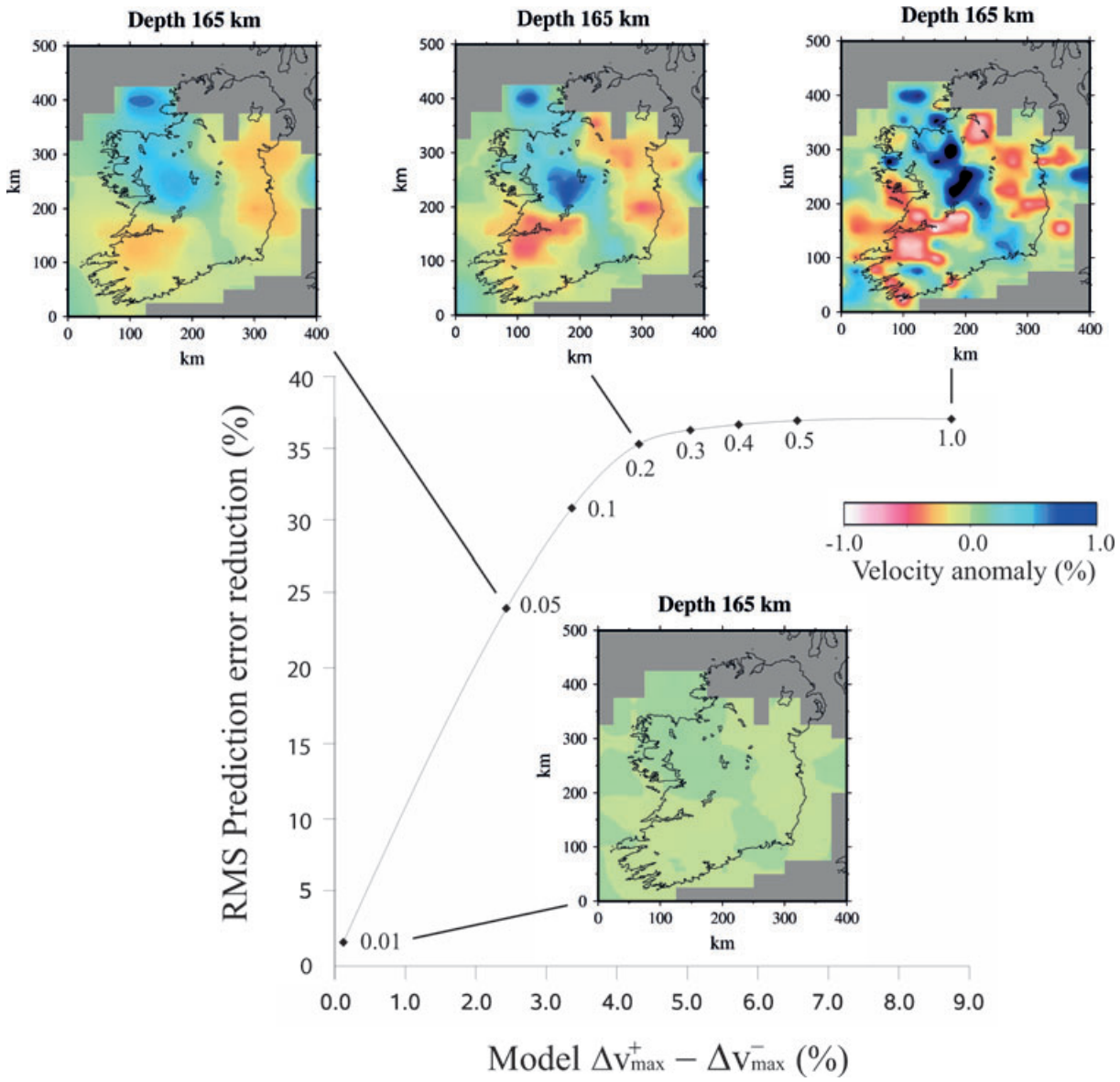

Figure A1. Trade-off curve showing the balance between model roughness (quantified by the difference between the extremal positive and negative velocity contrasts, $\Delta v^{+}_{max} - \Delta v^{-}_{max}$) and root mean square (rms) prediction error reduction, as a function of velocity model parameter standard deviations. Each point represents a model solution corresponding to the indicated model parameter standard deviations.

Fig. A2 illustrates the trade-off between density model roughness and gravity data fitting in the joint inversion, as a function of density model smoothing value. A value of 0.0002 was chosen from the 'knee' of the trade-off curve, representing a minimal structure solution for an rms prediction error reduction close to the maximum obtainable.

To illustrate the influence of the velocity–density relationship, *P*-wave model slices from pure traveltime and joint inversions are compared in Fig. A3. The high degree of correlation between the velocity models illustrates that it is the individual traveltime and gravity data sets which dominate the respective velocity and density models. The principal of joint inversion, however, is to return models which exhibit a consistency across both parent data sets. This is evident at depth slice 60 km of the joint inversion velocity model: as a result of the gravity low in west/northwest Ireland, the velocity model in this region has adapted slightly so as to yield consistent velocity and density models. Elsewhere at this depth, significant adaptation was not required because the gravity and traveltime signals were already largely in agreement, a result which we contend supports the applicability of a linear velocity–density relationship to the subcrustal Irish lithosphere. For the deeper slices, the gravity signal has diminished to such an extent that the travetime signal takes charge, leading to almost identical traveltime tomography and joint inversion velocity models. The approximately 1 per cent standard deviation employed for the B-coefficients evidently neither over-imposes (velocity and density models morphologically identical) nor under-imposes (velocity and density models structurally independent) the velocity–density relationship constraint. This additional constraint to be met in the joint inversion does, however, result in diminished recovered amplitudes compared with the pure traveltime tomography result.

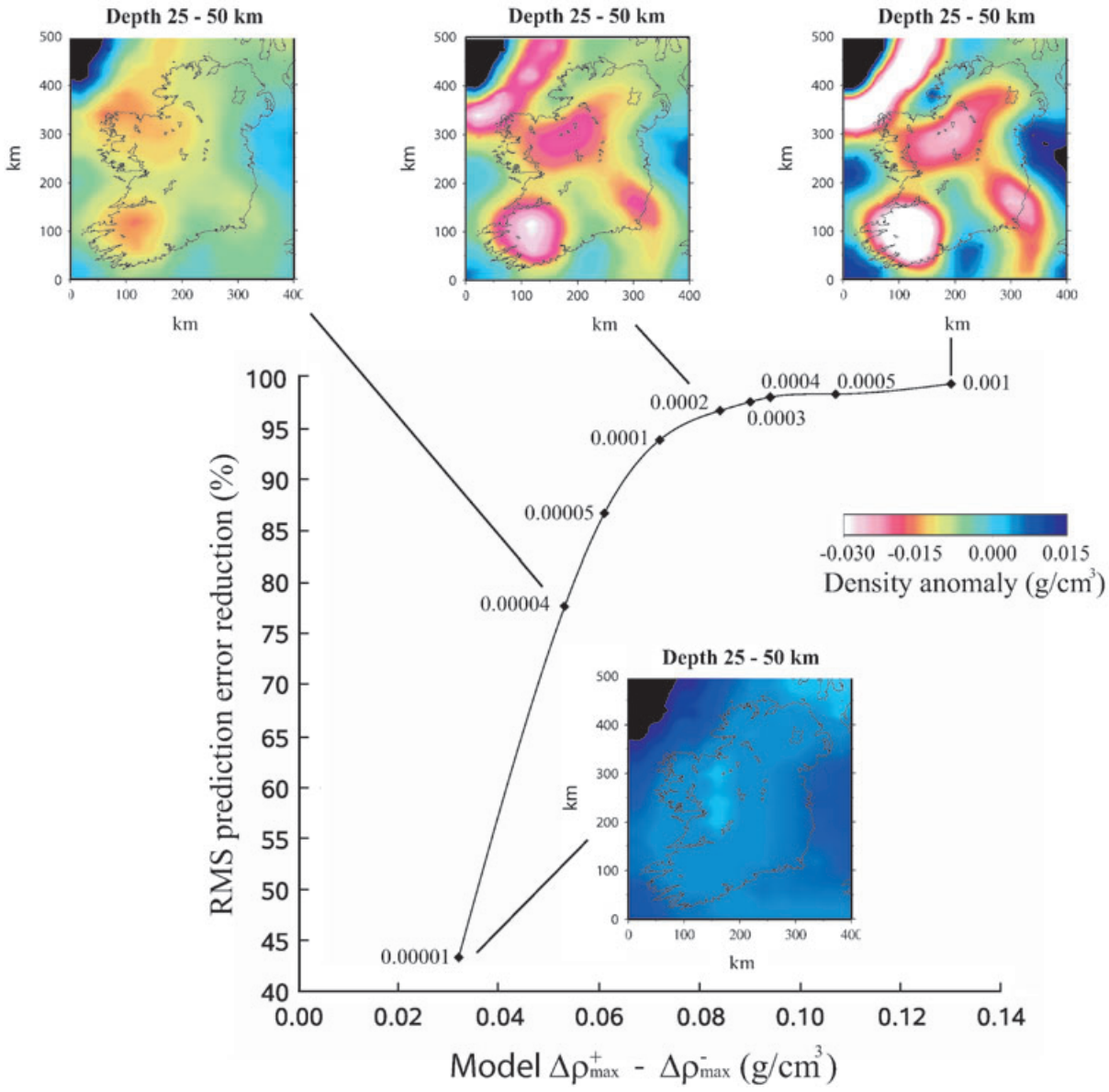

Figure A2. Trade-off curve showing the balance between density model roughness (quantified by the difference between the extremal positive and negative density contrasts, $\Delta\rho^{+}_{\max} - \Delta\rho^{-}_{\max}$) and gravity data fitting in the joint inversion, as a function of density model smoothing value. Each point represents a density model solution corresponding to the indicated smoothing value.

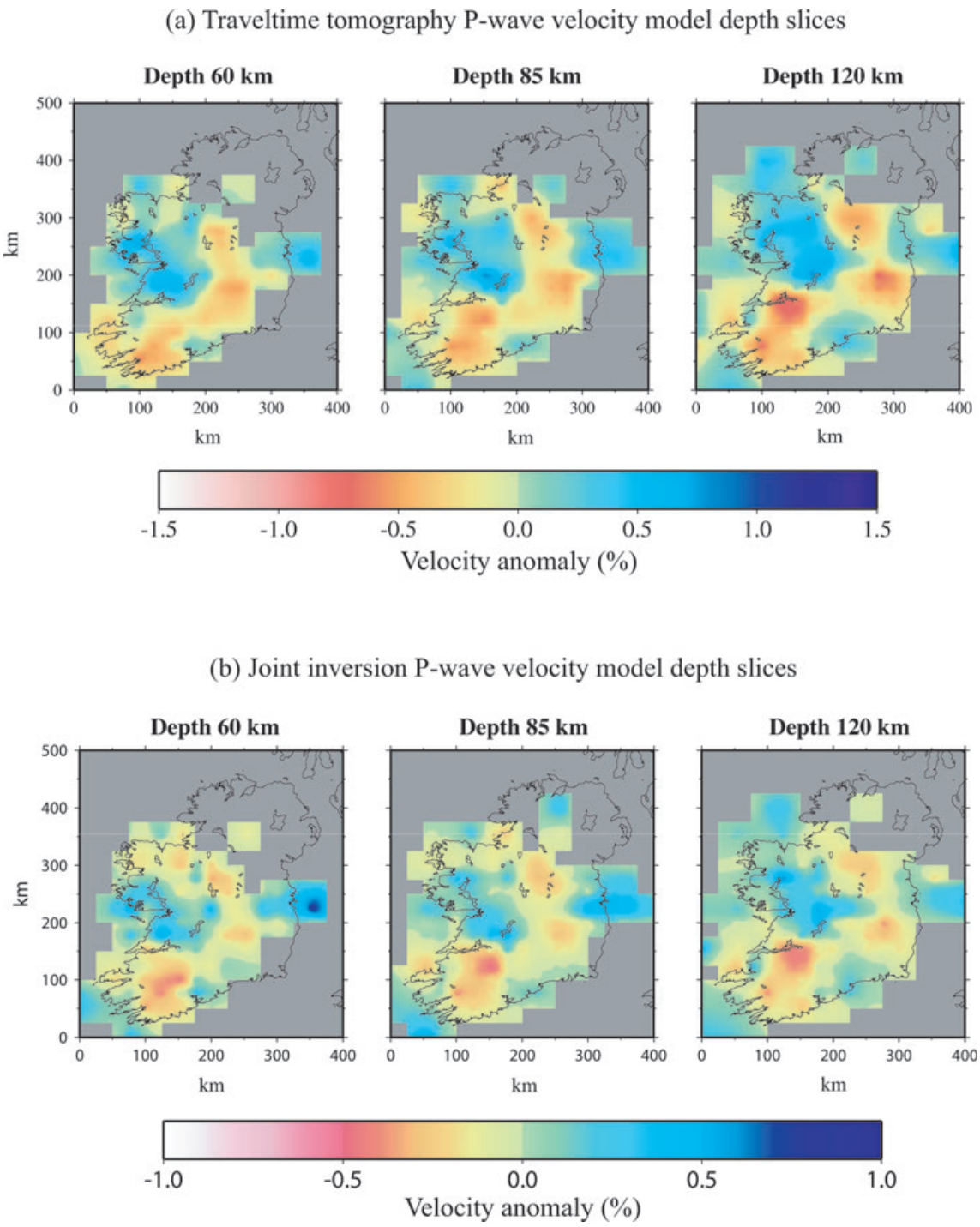

Figure A3. Comparison of *P*-wave velocity model slices derived from (a) pure traveltime tomography and (b) joint inversion.